Dissolution precipitation creep as a process for the strain localisation in mafic rocks

Amicia L Lee, Holger Stünitz, Mathieu Soret, Matheus Ariel Battisti

Journal of Structural Geology 155 (2022) 104505

Contents lists available at ScienceDirect

Journal of Structural Geology

journal homepage: www.elsevier.com/locate/jsg

Dissolution precipitation creep as a process for the strain localisation in mafic rocks

Amicia L. Lee [a,*], Holger Stünitz [a,b], Mathieu Soret [b], Matheus Ariel Battisti [c]

[a] Department of Geosciences, UiT – Arctic University of Norway, Norway
[b] Institut des Sciences de la Terre (ISTO), Université d'Orléans, France
[c] Instituto de Geociências, Universidade Federal do Rio Grande do Sul, Brazil

ARTICLE INFO

Keywords:
Amphibole
Mafic
Deformation
Diffusion creep
Dissolution precipitation creep
Strain localization

ABSTRACT

The lower crust is, on average, mafic in composition and composed of minerals that remain mechanically strong up to high temperatures. Here we show that dissolution-precipitation creep (as a type of diffusion creep) plays a major role in deformation of gabbro bodies at upper amphibolite facies conditions. The Kågen gabbro, N. Norway, is comprised of undeformed gabbro lenses enclosed by mylonitised margins that deformed at 690 ± 25 °C and 1.0–1.1 GPa. The evolution of the microstructures and fabric of the low strain gabbro to high strain margins were investigated. Original clinopyroxene and plagioclase dissolved during mineral reactions and precipitated as new minerals phases: new plagioclase and clinopyroxene (different compositions relative to the magmatic parents) and additional amphibole and garnet. Microstructural and crystallographic preferred orientation (CPO) data indicate that dissolution-precipitation creep is the dominant deformation mechanism. Amphibole shows a strong CPO that is primarily controlled by orientated growth in the stretching direction. The progression of mineral reactions and weakening is directly connected to a fluid-assisted transformation process that facilitates diffusion creep deformation of strong minerals at far lower stresses and temperatures than required by dislocation creep. Initially strong lithologies can become weak, provided that reactions proceed during deformation.

1. Introduction

Strain localisation and fabric development in the lower continental and oceanic crust are controlled by the active deformation mechanisms. The lower continental and oceanic crust are, on average, mafic in composition and primarily composed of plagioclase, pyroxene and/or amphibole (Rudnick and Fountain 1995), minerals that have been shown experimentally to remain mechanically strong up to high temperatures (Mauler et al. 2000; Bystricky and Mackwell 2001; Rybacki and Dresen 2004; Moghadam et al. 2010). Understanding the mechanisms of such deformation is the prerequisite to quantify the stresses, rates of deformation processes, and to infer general conditions and environment of the tectonic setting of lower crustal rocks.

Viscous deformation in the crust occurs primarily by two mechanisms; (1) dislocation creep and (2) diffusion creep combined with grain boundary sliding (GBS; e.g. Poirier 1985; Jessell 1987; Drury and Urai 1990; Wheeler 1992; Berger and Stünitz 1996). Dislocation creep involves intracrystalline deformation, where dislocations move through the crystal structure by processes of glide. Climb is required to minimise the internal strain energy resulting from dislocation glide (Carter and Ave'Lallemant 1970; van Roermund and Lardeaux, 1991; Platt and Behr 2011). The process of diffusion creep is the result of solid-state diffusion of atoms (diffusive mass transfer) through a crystal lattice, termed Nabarro-Herring creep, or along grain boundaries, termed Coble creep (Poirier 1985; Wheeler 1992; Langdon 2006). If diffusion is combined with dissolution in and precipitation from an aqueous fluid, pressure solution allows material to be transported along grain boundaries in a fluid film rather than the movement of atoms and vacancies (Rutter 1983). Coble creep and pressure solution are efficient processes at lower temperatures than Nabarro-Herring creep and are far more likely to be dominant in crustal materials (Elliott 1973; Poirier 1985). Dissolution-precipitation creep (DPC) is a term generally used for the process of dissolving and precipitating material during diffusion creep. DPC can occur within a single phase or it may be accompanied by metamorphic reactions. In the latter case the material is precipitated as new phase(s), resulting in transformation weakening (Stünitz 1993;

* Corresponding author.
E-mail address: amicia.lee@uit.no (A.L. Lee).

https://doi.org/10.1016/j.jsg.2021.104505
Received 6 August 2021; Received in revised form 22 December 2021; Accepted 28 December 2021
Available online 1 January 2022

Okudaira et al. 2015; Marti et al. 2017; Stünitz et al. 2020; Mansard et al. 2020a).

Amphibole and plagioclase are common mid to lower crustal minerals and as a consequence they are considered to play a large role in controlling the strength of crustal scale structures (Rudnick and Fountain 1995; Tatham et al. 2008; Lloyd et al. 2011). The strength and active deformation mechanisms of plagioclase at mid to lower crustal conditions have been the subject of many studies (e.g. Marshall and McLaren 1977; Tullis 1983; Dimanov et al. 1999; Kruse et al. 2001; H. Stünitz et al. 2003; Rybacki and Dresen 2004; Terry and Heidelbach 2006; Miranda et al. 2016), yet the rheology of mafic minerals have received little attention so far (Bystricky and Mackwell 2001; Dimanov et al. 2003, 2011; Dimanov and Dresen 2005; Moghadam et al. 2010), and that of amphibole remains poorly understood.

Experimentally, amphibole is considered to be strong at lower crustal conditions (Brodie and Rutter, 1985; Shelley, 1994), and only exhibits weakening with mechanical twinning and dislocation glide at high stresses and strain rates (Rooney et al. 1970, 1975; Dollinger and Blacic 1975; Morrison-Smith 1976; Hacker and Christie 1990). Amphibole exhibits a fabric during diffusion creep and reaction (Getsinger and Hirth 2014). Naturally deformed amphiboles have been shown to display brittle deformation at greenschist to amphibolite facies conditions (Allison and La Tour 1977; Brodie and Rutter 1985; Nyman et al. 1992; Stünitz 1993; Babaie and La Tour 1994; Imon et al. 2004; Soret et al. 2019). Evidence for crystal plasticity has been interpreted (often based upon CPO) in natural samples at temperatures from 450 to >650 °C via dynamic recrystallization, dislocation creep on (100)[001] and subgrain formation by dislocation glide (Biermann and van Roermund, 1983; Cumbest et al. 1989; Skrotzki 1992; Siegesmund et al. 1994; Díaz Aspiroz et al. 2007; Pearce et al. 2011). Additionally, evidence for diffusion creep of natural amphibole has been inferred by dissolution-precipitation creep and/or diffusion-accommodated GBS forming strong fabrics at upper greenschist to upper amphibolite facies conditions (Berger and Stünitz 1996; Imon et al. 2002, 2004; Okudaira et al. 2015; Giuntoli et al. 2018; Soret et al. 2019; Graziani et al. 2020; Mansard et al. 2020a; 2020b). Naturally deformed amphibole usually produces strong fabrics and is thought to be responsible for the strongly anisotropic lower crust (Mainprice and Nicolas 1989; Tatham et al. 2008; Lloyd et al. 2011; Ji et al. 2013).

From the short summary of literature results above, it emerges that the relationships between chemical reactions, fabric formation, and deformation mechanisms in mafic rocks are poorly understood, yet they play a major role for understanding the mechanical strength of the crust and for localizing deformation in different tectonic settings. In this study, we analyse the microstructures and chemistry of the deformed margin of the Kågen gabbro (N. Norwegian Caledonides) to show the influence of mineral reactions and fluids on active deformation mechanisms and strain localisation during deformation at amphibolite facies conditions.

2. Geological setting

The Caledonides formed from convergence and collision of Baltica and Laurentia during the Silurian to Devonian periods. In northern Norway, large-scale nappe stacking preserves a section of autochthonous Baltica basement and ophiolites with varying metamorphic grades and deformation style (Corfu et al. 2014). The Reisa Nappe Complex (from bottom to top: Vaddas, Kåfjord, and Nordmannvik nappes; Fig. 1a) in northern Troms is considered to be Iapetus-derived or part of the outer Baltica margin (Andersen et al. 1982; Corfu et al. 2006). It underwent viscous deformation and metamorphism at amphibolite-to granulite-facies conditions with pervasive partial melting (Roberts and Sturt 1980; Faber et al. 2019).

The Kågen gabbro intruded into amphibolite to granulite-grade metasediments of the Vaddas Nappe and is exposed on the islands of Kågen and Arnøya (Fig. 1b). The emplacement of the gabbro occurred at 439 ± 1 Ma (U–Pb zircon concordia age; Faber et al. 2019), and cooling is recorded over a broad temperature range of 650–900 °C at pressures of 0.7–0.9 GPa that correspond to depths of 26–34 km resulting in partial melting of the adjacent felsic and metapelitic rocks (Getsinger et al. 2013; Gasser et al. 2015; Faber et al. 2019). A mantle melt source and extensional setting is implied from the tholeiitic composition of the

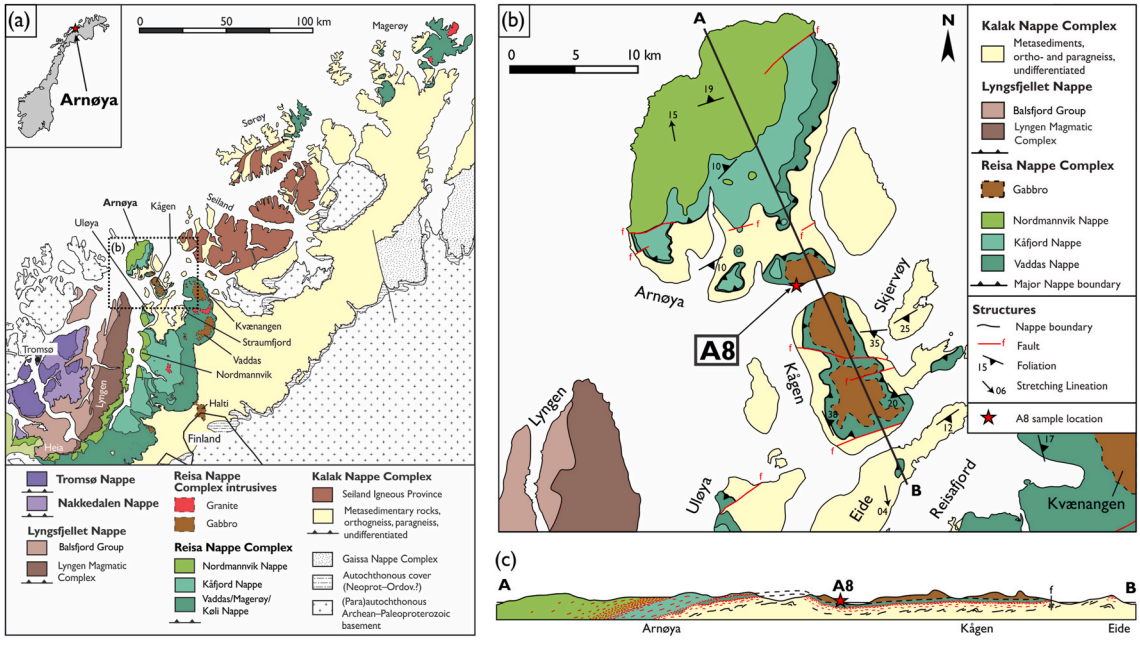

Fig. 1. Geological map of the study area in Northern Norway. (a) North Norwegian Caledonides focussing on the Tromsø to Kalak Nappe Complexes. (b) Detailed map of Arnøya and Kågen to highlight the sample area in the Kågen gabbro. (c) Cross section through Arnøya and Kågen showing the gabbro intruded into the Vaddas Nappe. The density of red lines corresponds to the intensity of ductile deformation within and along boundaries between individual nappes. Caledonian foliations are shown in red, whereas black ones are possibly pre-date Caledonian deformation. After Faber et al. (2019). (For interpretation of the references to colour in this figure legend, the reader is referred to the Web version of this article.)

gabbro in the Vaddas Nappe (Lindahl et al. 2005).

The sample location is situated near the western margin of the Kågen gabbro on Arnøya (GR: 70.04389N, 20.71444E). The outcrop region consists of undeformed gabbro lenses with mylonitised margins enveloping the lenses (Fig. 2a), and is approximately 0.7 km west of samples studied by Getsinger et al. (2013). The area studied by Getsinger et al. (2013) hosts several hydrous pegmatite intrusions that locally hydrated the gabbro and partitioned deformation during emplacement of the gabbro. The deformed margins of gabbro pods in our sample area are not associated with pegmatite intrusions, and, together with the formation of a regional fabric close to margin of the gabbro body, indicate a different setting for the deformation.

The Vaddas Nappe underwent shearing at 432 ± 6 Ma (TIMS, mean $^{206}Pb/^{238}U$ age in titanite), temperatures of 630–640 °C, pressures of 1.2–1.3 GPa and depths 43–46 km during the main Scandian collision event of the Caledonides (Faber et al. 2019), and the gabbro outcrops of this study have been deformed during this orogenic stage. This paper investigates the processes occurring during deformation of mafic rocks and where the observed deformation in the Kågen gabbro is related to the Vaddas Nappe and Caledonian deformation history.

3. Methods of study

In this paper we analysed polished thin sections in order to investigate the features of strain variation through sample A8B described below (Fig. 2c, Table 1). The sample is cut in the X-Z section of the kinematic reference frame, where the X-axis is pointing to the plunging direction of stretching lineation (NW) and Z-axis pointing towards the pole of the foliation. Where minerals have been abbreviated, we follow the database from Whitney and Evans (2010).

3.1. Electron microscopy

Electron probe microanalysis was carried out at CAMPARIS (Sorbonne University, Paris, France) using a Cameca SX-Five instrument. Point measurements were made using 15 kV accelerating voltage, a 10 nA beam current with a 1 μm spot size. Composition maps were acquired using a 15 kV accelerating voltage, a 40 nA beam current with a 1 μm spot size and 50 ms dwell time. The instrument was calibrated using diopside (Ca, Mg, Si), MnTiO3 (Mn, Ti), orthoclase (K, Al), Fe2O3 (Fe), albite (Na) and Cr2O3 (Cr) as standards to measure elements in brackets. Selected representative analyses of garnet, clinopyroxene, plagioclase and amphibole from point analysis are shown in Table 2.

3.2. Thermodynamic modelling and empirical thermo-barometry

Several empirical thermo-barometers were used to estimate the pressure-temperature conditions of formation of the mineral assemblages observed in the low, mid and high strain zones. The crystallization temperatures of metamorphic garnet and clinopyroxene pairs at microstructural equilibrium were estimated using the thermometer of Powell (1985). For these estimates, pressure was taken to be ~1 GPa - a conservative assumption as garnet–clinopyroxene thermometry is poorly dependent on pressure (pressure variations of 0.5 GPa affect the temperature by ≤ 15 °C). The crystallization temperatures of amphibole and plagioclase pairs were calculated using the combined thermo-barometers of Holland and Blundy (1994) and Molina et al. (2015).

In addition, forward thermodynamic modelling (Perple_X software version 6.8.6; (Connolly and Kerrick 1987; Connolly 2009) were conducted to estimate the pressure-temperature conditions of the high

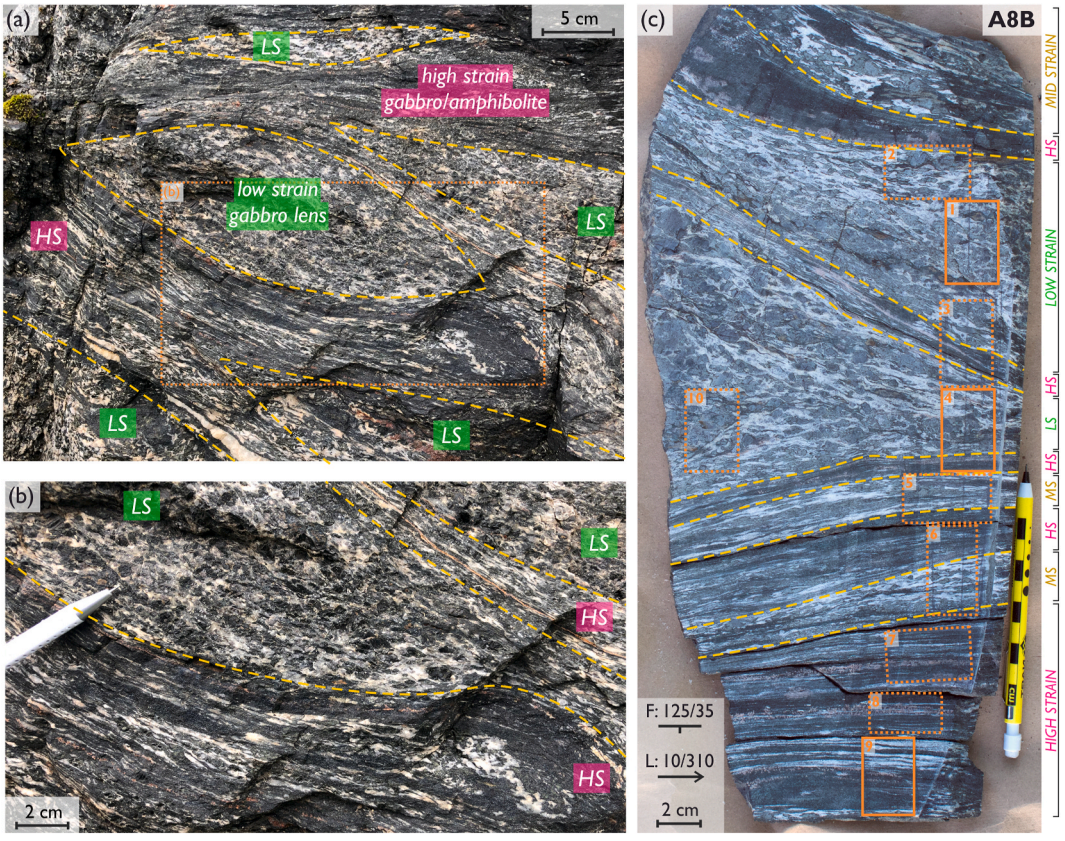

Fig. 2. (a) Outcrop photograph of sample area (GPS: 70.04387°N, 20.71438°E), boundaries between low and high deformation areas highlighted by yellow dashed lines. (b) Detailed photograph from (a) with deformation boundaries and low/high strain zones identified. (c) Photograph of sample A8B with thin section locations highlighted by orange boxes, deformation boundaries between low, mid and high strain zones identified. LS, low strain; MS, mid strain; HS, high strain. (For interpretation of the references to colour in this figure legend, the reader is referred to the Web version of this article.)

strain layers. In contrast to the low and mid strain domains, the high strain domain showed clear criteria of chemical equilibrium. The pseudosection was modelled in the NCKFMASH system using the internally consistent thermodynamic dataset (hp62ver.dat) of Holland & Powell (2011). The following solution models were used: White et al. (2014) for orthopyroxene, biotite, chlorite and garnet, Green et al. (2016) for mafic melts, augite and hornblende, and Holland and Powell (2003) for plagioclase and K-feldspar. The H_2O value was set to 1.1 wt % after calculating a T-X(H_2O) diagram with a H_2O content ranging from 0.5 to 2 wt% (i.e., excess water) at a pressure of 1 GPa, consistent with the estimates from the amphibole-plagioclase thermo-barometry (Fig. S1, Table S1; Holland and Blundy 1994; Molina et al. 2015). The H_2O value is also consistent with the proportion of amphibole (~50 vol %) observed in the high strain layers (see section 4.1.3).

3.3. Electron backscattered diffraction (EBSD)

Crystallographic orientation data was collected via electron backscattered diffraction (EBSD) Oxford Instruments Nordlys S detector also on the Zeiss Merlin SEM at the University of Tromsø. Crystallographic data were collected using 20 kV accelerating voltage, 70° specimen tilt angle and 24–29 mm working distance. Detailed maps of ~16 mm^2 were measured with a step size of 1–3 μm and 7 bands detected. Oxford Instruments Aztec software was used for data acquisition and initial data processing, MTEX v.5.2.8 open source software toolbox (Bachmann et al. 2010) for MATLAB was used for enhanced data processing and pole figure plotting. Individual crystal orientations with median absolute deviation (MAD) values > 1.0 were removed. Individual grains were reconstructed using the 'calcGrains' function in MTEX using a 10° misorientation cut-off relative to neighbouring solutions. Pole Figures were created for the mean orientation of each grain based on the orientation distribution function (ODF), using the 'calcDensity' function within MTEX (Bachmann et al. 2010). The mean orientation of each individual grain was then plotted on lower hemisphere, equal area pole figures such that each data point represents a single grain on the pole figure, which are subsequently contoured. Calculated J-indices show the CPO fabric strength (e.g. e.g. Bunge 1982; Mainprice and Silver, 1993) and the M-indices shows the misorientation index (e.g. Skemer et al., 2005).

3.4. Grain shape parameters

Grain size and shape parameters are measured using grains calculated from the EBSD map data as described above with a misorientation threshold of 10°. The grain size is calculated via the equivalent radius (derived from the grain area) and multiplied by 2 to yield the grain size. The grain data for low, mid and high strain areas have been grouped together to give an overview of grain shape parameters in each of the strain zones (see Table 1 for strain domains). The histogram has 5 μm bin sizes and shows grain sizes up to 500 μm (larger grains are present in the samples but low in quantity). Grain statistics for mean, median, mode (range of largest bin) and standard deviation are shown alongside the grain size histogram data in. Grain orientation is calculated using a fitted ellipse and orientation of the long axis.

4. Results

4.1. Sample description

The outcrop displays strain gradients with weakly deformed low strain domains (5–20 cm in height, 20–40 cm in length) that are bound by high strain mylonites (Fig. 2). Even in the less deformed domains, the original gabbroic fabric described by Getsinger et al. (2013; c.700 m east) is not or only partially preserved (Fig. 2). Mid-strain domains show segregation of mafic and plagioclase-derived minerals, and this distinction develops into thin layers in most high strain zones (Fig. 2c). Below, we present the results for microstructures, chemical properties and crystallographic preferred orientation (CPO) of each type of domain (low, mid and high strain zones). Strain domains present in each thin section and EBSD map are summarised in Table 1.

The heterogeneous strain distribution typically shows the highest strain parts between lower strain parts. Such a strain distribution is interpreted as a narrowing of shear zones caused by progressive localisation of deformation (type 2 shear zone; Means 1995). This interpretation implies that lower strain regions preserve earlier stages and the highest strain regions the last stages of the deformation history.

4.1.1. Low strain zones

The primary phases in the low strain zones are clinopyroxene and plagioclase with minor orthopyroxene, amphibole ilmenite and zoisite (Fig. 3a). The original igneous gabbro assemblage has been metamorphosed; original pyroxene porphyroclasts (referred to as cpx_1) are surrounded by a mixing of secondary pyroxene (cpx_2) and amphibole (amp_A) grains forming corona rim structures. New plagioclase grains (pl_2) replace original plagioclase grains (pl_1; Fig. 4a–c, 6c).

The cpx_1 grains are much larger in size (3–6 mm) than the cpx_2 grains (<200 μm). The cpx_1 show undulose extinction and thin lamellae of ilmenite and amphibole reaction products (amp_A) along cpx_1 cleavage planes/cracks (Fig. 3a and b, 4a-b). Some large cpx_1 grains have neocrystallized portions that follow larger cleavage cracks in the original grain; these are composed of both cpx_2 and amp_A (Fig. 4a and b).

The amp_A grains have a larger grain size in the cpx_1 strain pressure shadows, 50 vs. 100 μm (Fig. 4a–f, 5a). Shape and size analysis of amphibole grains show a unimodal grain size distribution with a mean grain size of 68 μm and grains are elongated parallel to the foliation

Table 1
Summary of strain domains present in each thin section. Dominant strain domain present in EBSD maps is shown below the relevant host thin section.

Thin Section	Strain domain present		
EBSD map	Low	Mid	High
A8B1	**Y**		
1a	Y		
1b	Y		
A8B2	**Y**		
2a	Y		
2b	Y		
A8B3	**Y**	**Y**	**Y**
3a	Y		
3b			Y
3c		Y	
3d			Y
A8B4	**Y**	**Y**	**Y**
4a		Y	
4b		Y	
4c			Y
A8B5		**Y**	**Y**
5a		Y	
5b		Y	
A8B6	**Y**	**Y**	**Y**
6a		Y	
A8B7			**Y**
7a			Y
7b			Y
A8B8			**Y**
8a			Y
A8B9			**Y**
9a			Y
9b			Y
A8B10	**Y**		
10a	Y		
10b	Y		

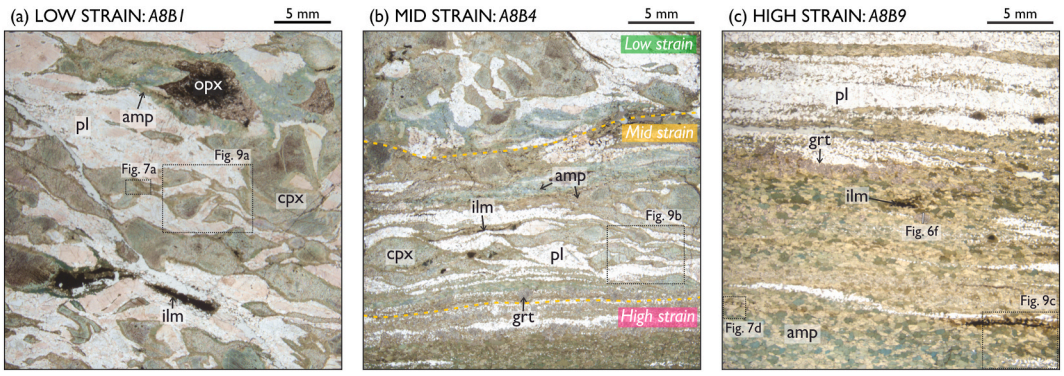

Fig. 3. Overview thin section photomicrographs of representative (a) low, (b) mid and (c) high strain areas in sample A8B. (a) The low strain area shows clinopyroxene grains surrounded by amphibole coronas. Areas of chemical analysis (Fig. 7a) and EBSD (Fig. 9a) are indicated. (b) A characteristic mid strain area bound to the top by a low strain zone, and below by a high strain domain. Amphibole replacement of clinopyroxene is more extensive and plagioclase is highly recrystallized. Box Fig. 9b indicates area of EBSD analysis. (c) High strain region with amphibole and plagioclase layers. Garnet profile for Fig. 6f and EBSD map area for Fig. 9c are indicated.

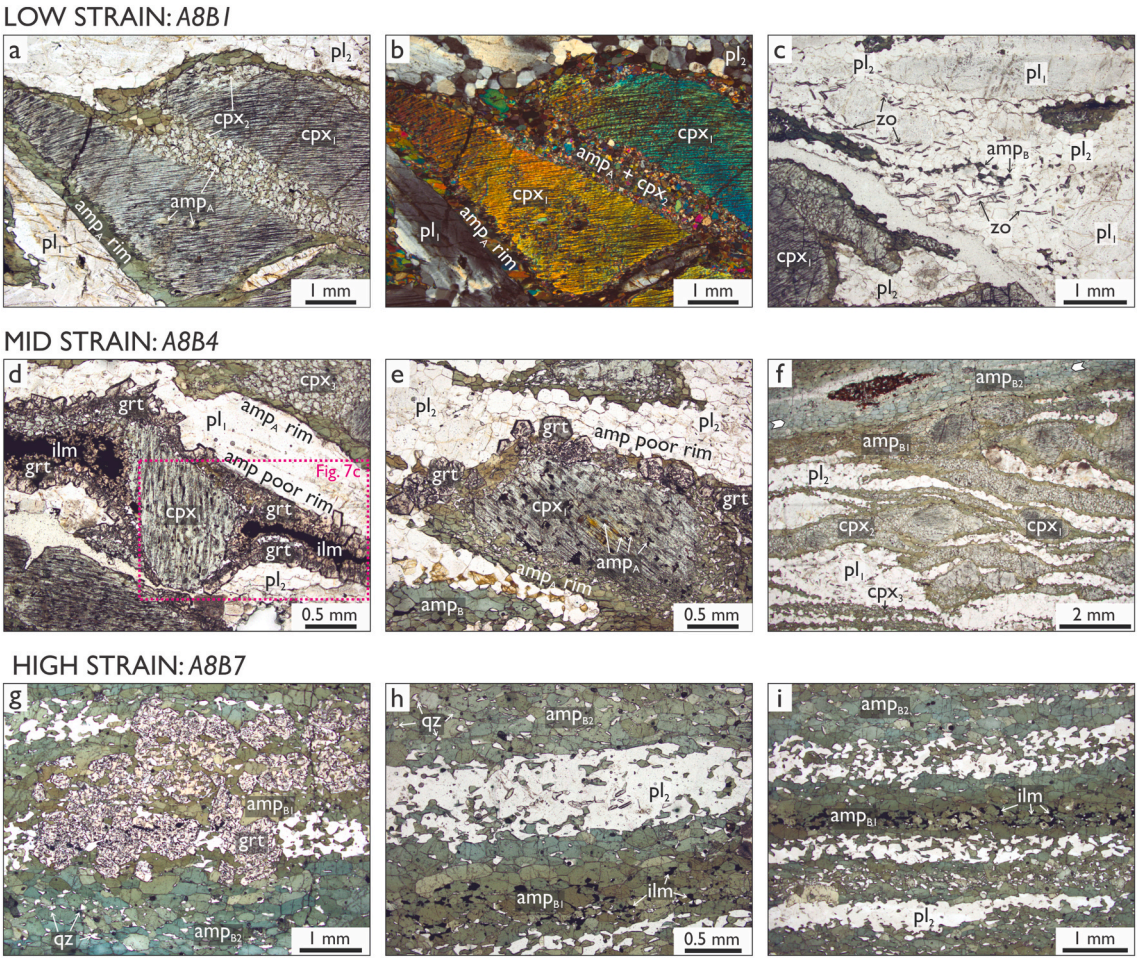

Fig. 4. Detailed thin section photomicrographs of specific textures in (a–c) low, (d–f) mid and (g–i) high strain areas in sample A8B. Low strain: (a–b) clinopyroxene grain with recrystallized fracture and amphibole rim; (c) zoisite and isolated amphibole grains with pl_1 and pl_2 plagioclase grains. Mid strain: (d) cpx1 grain with garnet rim, rim reaction is amphibole poor; (e) clinopyroxene grain with garnet rim on the top and amphibole rim below; (f) amphibole replacement of clinopyroxene, top section between arrows shows complete amphibole replacement, below this original clinopyroxene grains are still preserved. High strain: (g) garnet within amphibole zone; (h–i) amphibole-plagioclase layers, amphibole is olive green coloured when associated with ilmenite (amp_{B1}) and otherwise jade green coloured (amp_{B2}). All photomicrographs are in plane polarized light except (b) that is under cross-polarised light. (For interpretation of the references to colour in this figure legend, the reader is referred to the Web version of this article.)

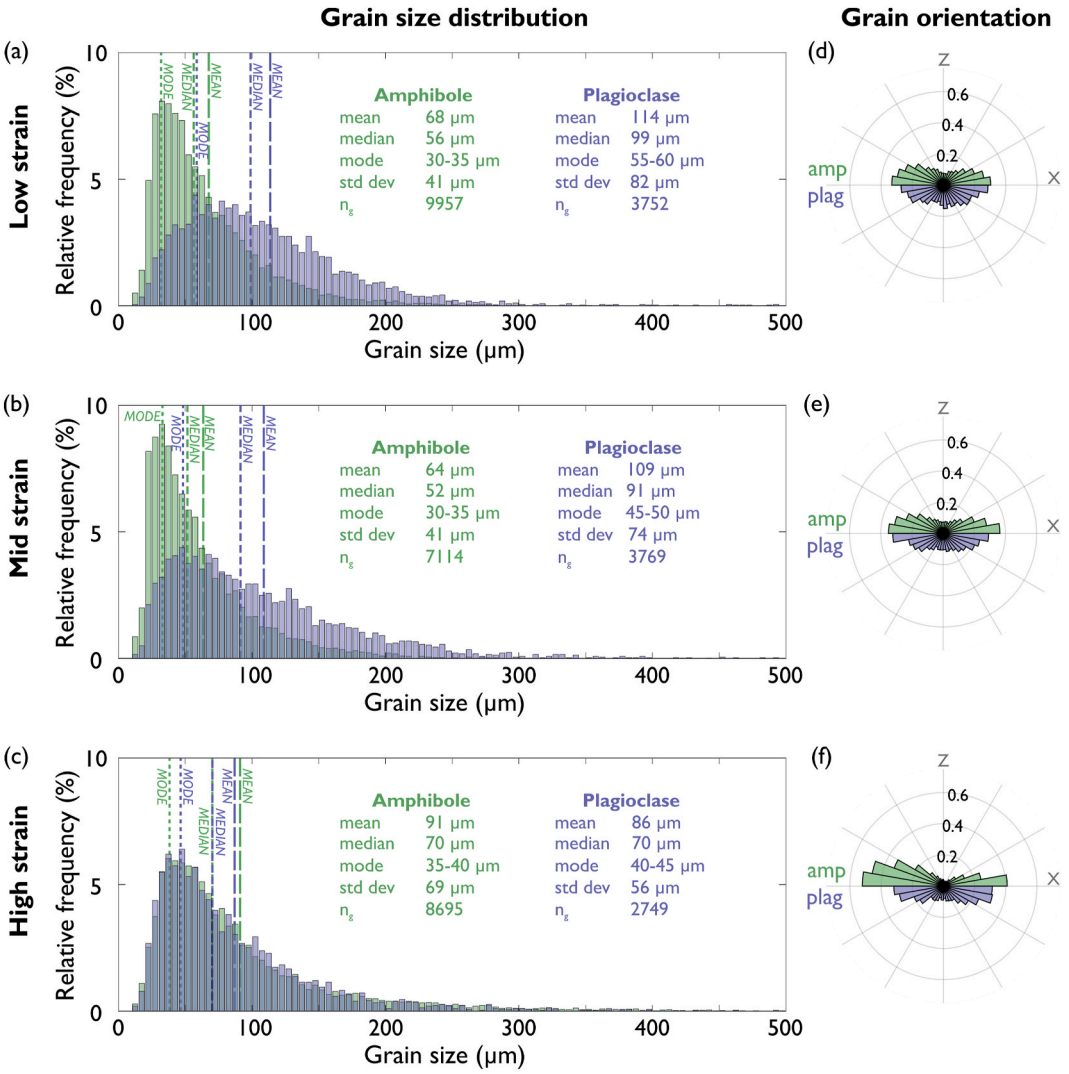

Fig. 5. Grain size and shape properties for amphibole and plagioclase grains. (a–c) Grain size distribution with grain statistics for amphibole and plagioclase grains in low to high strain areas of the sample. (d–f) Normalised grain orientation or shape preferred orientation of amphibole and plagioclase grains in low to high strain areas. Grain data for each strain area is grouped together, low strain data includes data from EBSD maps 1a, 1b, 2a, 2b, 3a, 10a and 10b; mid strain data includes EBSD maps from 3c, 4b, 4c, 5a, 5b and 6a; and high strain data includes EBSD maps from 3b, 3d, 4a, 7a, 7b, 8a, 9a and 9b. Number of grains considered for each strain area is indicated by n_g. The frequency for rose diagrams is 0–1 and grain orientation is in the kinematic reference frame (the same as CPO pole figures in Figs. 9–11).

(Fig. 5a, d). The orthopyroxene grains have also been replaced by amphibole; the few relicts that remain are fully recrystallized (Fig. 3a).

The original pl_1 grains are up to 3 mm with undulose extinction. They generally include zoisite needles up to 400 μm in length (Fig. 4b and c, 6c). The later neo-crystallized pl_2 grains are recrystallized 50–300 μm in size and show straight extinction and ~120° triple junctions (Fig. 4b and c). The plagioclase domains typically appear more deformed than the pyroxene domains and form a weak foliation.

Ilmenite is found adjacent to clinopyroxene grains and often exhibits amphibole or garnet coronas rims (Figs. 3a and 4d). Olivine is not found in the A8B sample, but it is present in undeformed gabbro ~700 m east as detailed by Getsinger et al. (2013).

4.1.2. *Mid strain zones*

Towards the margins of the gabbro pods, the foliation is progressively stronger in intensity (Fig. 3b). Clinopyroxene, plagioclase and amphibole are the dominant phases with minor amounts of garnet, zoisite, quartz and ilmenite whilst orthopyroxene is not present. Corona structures are ubiquitous and grade into elongated tails at the ends of porphyroclasts defining the foliation.

Cpx_1 grains represent the primary grains and are 0.5–2 mm in size (smaller than in the low strain areas of the rock). The primary cpx_1 grains have undulose extinction and the thin lamellae of amp_A along cpx_1 cleavage planes can be recrystallized as 'blebs'. The recrystallized tails consisting of new grains of cpx_3 have a granoblastic texture without signs of internal grain deformation (top right of Figs. 4d, 5b-c).

The amp_A grains that surround both cpx_1 grains and cpx_2 grains from recrystallized tails are coarser than in low strain domains, up to 200 μm. Quartz is present in trace volumes between some cpx_1 grains and their surrounding amp_A rims (Fig. 6c). There are zones where amphibole (amp_B) has almost completely replaced the cpx_1 (e.g. amp_{B2} zone in Fig. 4f). In these elongated zones of bands the amp_B grain size is up to 500 μm. Within these bands, there are minor amounts of clinopyroxene, quartz and ilmenite. Despite the observed grain size increase in amphibole, the average grain size is only 64 μm as there is a high proportion of small amp_A grains associated with the clinopyroxene replacement (cpx_2; Fig. 4d–f, 5b).

Similarly to the cpx_1, the large pl_1 grains are smaller in the mid strain zone (up to 2 mm), although still exhibit undulose extinction and deformation bands. The recrystallized pl_2 grains show little internal

deformation. Some grain boundaries are more lobate than in the low strain zones (Figs. 4e and 6c). The amphibole and plagioclase grains in the mid strain areas are orientated with their long axes parallel to the foliation (Fig. 5e). Prismatic zoisite is up to 500 μm in length within large pl_1 grains where they are loosely aligned to the foliation but zoisite is also present in the smaller pl_1 grains with a random orientation (Fig. 4c, e). In some mid strain regions garnet grows in bands after cpx_1, pl_1 and ilmenite, the grains are up to 100 μm in size, are faceted and have equant shape with quartz inclusions (Fig. 4d and e).

4.1.3. High strain zones

In several layers around the gabbro pods and in between the mid strain zones, there are high strain zones, where the rock is strongly deformed and appears mylonitic in the field (Fig. 2). The foliation is well developed in the high strain zones exhibiting alternating bands of amphibole and plagioclase with occasional garnet bands (Fig. 3c). The amp_B bands have trace amounts of clinopyroxene, quartz, calcite, and ilmenite interspersed (Fig. 4g–i).

The amp_B grains are up to 600 μm in length with a mean grain size of

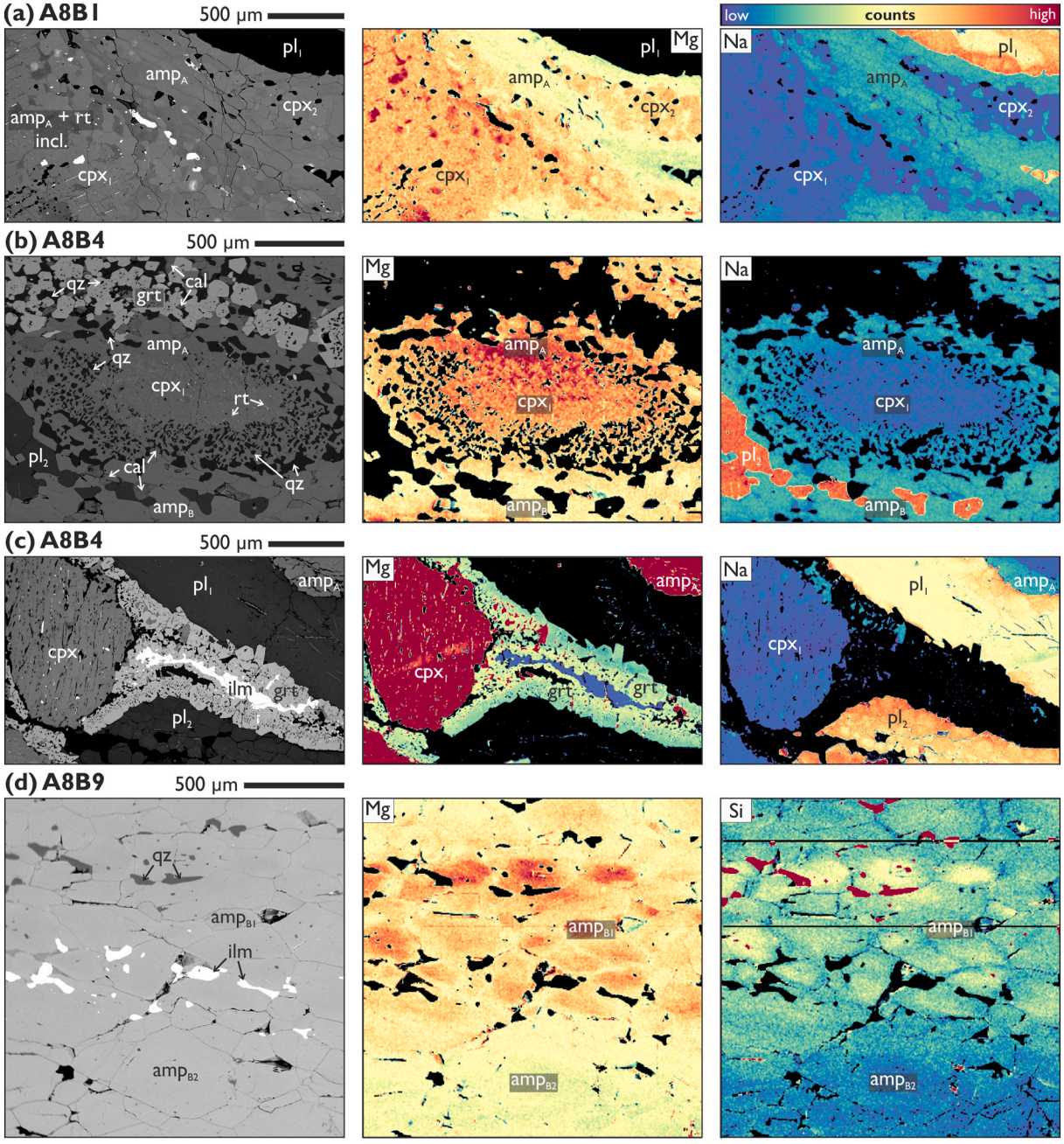

Fig. 6. BSE images and compositional maps of detailed microstructural features in (a) low, (b–c) mid and (d) high strain areas of the Kågen gabbro margins. (a) Edge of clinopyroxene grain from Fig. 3a, Mg and Na chemical maps highlight variations in clinopyroxene, amphibole and plagioclase chemistry. New small grains surrounding or forming tails around magmatic porphyroclasts have lower Mg and higher Na value than the original clinopyroxene grain (b) Clinopyroxene grain with amphibole replacement and garnet band, Mg and Na maps highlight variations in clinopyroxene and amphibole chemistry associated neighbour grains. (c) Amphibole-poor clinopyroxene grain from Fig. 4d. Mg map highlights the variation in garnet chemistry when adjacent to plagioclase (low) or clinopyroxene/ilmenite (high). Plagioclase shows elevated Na when adjacent to garnet or amphibole as opposed to the core of pl_1 grains. New pl_2 grains are also have a higher Na. (d) Amphibole band in a high strain region. Mg- and Si-rich cores in amp_{B1} (olive green coloured) compared to amp_{B2} (jade green coloured). (For interpretation of the references to colour in this figure legend, the reader is referred to the Web version of this article.)

91 μm (Fig. 5c). Amphibole in layers associated with garnet and ilmenite are olive green (amp_{B1}) in colour under plane polarized light, compared to amphibole layers with low volumes of minor minerals that are jade green (amp_{B2}) in colour (Fig. 4g–i). Amphibole shows the strongest SPO of the differently strained zones with grains strongly orientated parallel to the shear direction, and also to the foliation (Fig. 5f).

The pl_2 bands are recrystallized and no longer contain any of relicts of original pl_1 grains (porphyroclasts; Fig. 4g–i). Pl_2 is also present in mixed bands with amp_B, forming polyphase layers (Fig. 4i). In such layers, the mean plagioclase grain size is decreased to 83 μm and the grain size distribution is virtually identical to amphibole (Fig. 5c). The plagioclase grains show a similar long axis orientation in the mid and high strain areas (Fig. 5 e-f).

Quartz is present as interstitial blebs and inclusions within amphibole and plagioclase. Calcite and ilmenite are both cuspate in shape. Zoisite is rarely present in high strain zones. When found it is less than 20 μm long and randomly orientated (Fig. 4h). Garnet bands up to 4 mm in width are commonly associated with amphibole-plagioclase band alternation (Fig. 4g). Isolated garnet grains are also present within amphibole layers. The garnets are subhedral, typically 1–3 mm in size and are associated with quartz and calcite. Quartz is present as inclusions and interstitial blebs in the garnet whilst calcite is interstitial forming cuspate shapes around the garnets (Figs. 4g and 6b).

4.2. Mineral chemistry

Clinopyroxene has a diopside-rich composition with a Mg# [Mg/(Mg+Fe)] ranging between 0.65 and 0.80 (Fig. 6a, Table 2). Magmatic porphyroclasts of cpx_1 (samples A8B1, A8B4) show higher values (0.75–0.80) than new small cpx_2 grains at their rims and tails (0.75–0.72). New metamorphic cpx_3 grains scattered in the matrix (sample A8B4) show the lowest Mg# values (0.65–0.73). The amount of Na, representing the jadeite content, varies between 0.3 and 0.5 a.p.f.u. regardless of the microstructural position. The changes in Mg and Na content are illustrated in Fig. 6a and b, new small grains surrounding or forming tails around magmatic cpx_1 porphyroclasts have lower MgO and higher Na_2O value than the original cpx_1 grains. All chemical analyses are available in Table 2.

Amphibole analyses plot within the pargasite to actinolite fields (nomenclature from Leake et al. 1997, Fig. 7b). The Mg# varies between 0.50 and 0.75, and the Ti ranges up to 0.25 a.p.f.u (Fig. 7c, Table 2). The Mg# shows a continuous increase, and the Ti a continuous decrease versus increasing Si, with clear microstructural relations (Fig. 6). Amp_A crystallizing after the magmatic cpx_1 porphyroclasts in the low and mid strain zones (samples A8B1, A8B4) has the highest Mg# (>0.60) and Si values (>6.6 a.p.f.u.) and the lowest Ti content (<0.1 a.p.f.u.). In the low, mid and high strain zones, amp_B co-existing with pl_2 has lower Mg# (<0.63) and Si values (<6.6 a.p.f.u) with generally higher Ti content (0.06–0.16 a.p.f.u.). While amp_C included in garnet in the mid strain zone has the same composition as amp_B in the plagioclase-rich layers, amp_D included in garnet in the high strain zone shows the highest Ti content (0.12–0.24).

The plagioclase has an anorthite content [Ca/(Ca+Na)] varying between 0.25 and 0.60 (Fig. 7d). A correlation is observed with both microstructural position and fabric intensity. In the low (A8B1) and mid (A8B4) strain zone, the cores of magmatic pl_1 porphyroclasts (Fig. 6a) have the highest anorthite content (0.54–0.60). The prophyroclast rims and new small grains of pl_2 at microstructural equilibrium with amp_B in such samples (Fig. 6a, c) show an intermediate composition (values of 0.35–0.55). A similar distribution is observed for the new recrystallized pl_2 grains equilibrated with amp_B in the high strain zone (e.g. mixed amp-pl bands in Fig. 4h–c, 11c), varying from 0.28 to 0.45. Pl_3 in the garnet-amphibole bearing layers from the mid and high strain zones (samples A8B4, A8B9) have the lowest anorthite content (0.25–0.40).

The garnet chemical composition in the amphibole-free layers of the mid strain zones varies in function of the neighbouring minerals (Figs. 6 c, 7e-f). Regions near crystal faces next to clinopyroxene are enriched in Fe and Mg (Alm: 0.59, Prp: 0.15, Grs: 0.23, Sps: 0.02) while regions near faces next to plagioclase are enriched in Ca (Alm: 0.51, Prp: 0.10, Grs: 0.36, Sps: 0.02). Mn content remains low regardless of the neighbouring

Table 2
Selected representative analyses of garnet, clinopyroxene, plagioclase and amphibole from point analysis.

Min.	Grt	Grt	Grt	Cpx	Cpx	Cpx	Cpx	Pl	Pl	Pl	Pl	Pl	Amp	Amp	Amp	Amp
Thin section	A8B4	A8B4	A8B9	A8B1	A8B1	A8B4	A8B4	A8B1	A8B1	A8B4	A8B9	A8B9	A8B1	A8B4	A8B4	A8B9
Anal.	256/1	111/1	125/6	15/1	87/1	224/1	92/1	101/8	61/1	212/1	44/1	12/1	60/1	211/1	364/1	119/1
SiO_2	38.15	38.33	38.18	53.94	53.22	53.77	52.45	54.46	58.2	59.24	59.9	62.12	42.1	43.79	52.47	43.34
TiO_2	0.06	0.01	0.06	0.11	0.13	0.10	0.06	0.00	0.00	0.00	0.00	0.00	1.23	1.48	0.34	1.18
Al_2O_3	21.24	20.82	21.06	1.12	1.39	1.18	1.06	29.55	27.36	25.88	25.30	23.83	16.47	13.53	5.48	12.77
FeO	25.01	24.31	25.22	7.13	8.64	6.78	11.22	0.00	0.00	0.00	0.00	0.00	12.85	13.20	9.45	15.37
MnO	1.50	0.95	2.34	0.14	0.25	0.12	0.06	0.00	0.00	0.00	0.00	0.00	0.20	0.04	0.14	0.19
MgO	4.70	2.76	3.50	13.87	13.12	13.95	12.07	0.00	0.00	0.00	0.00	0.00	10.00	11.05	16.49	10.37
CaO	9.28	13.37	9.78	23.39	23.08	23.81	22.37	11.33	8.76	7.68	7.03	5.24	11.49	11.59	11.80	11.07
Na_2O	0.02	0.01	0.00	0.51	0.52	0.57	0.62	5.07	6.50	7.36	7.47	8.51	2.26	2.13	0.81	1.91
K_2O	0.00	0.00	0.04	0.00	0.00	0.00	0.00	0.00	0.05	0.07	0.09	0.06	0.46	0.43	0.09	0.46
Σ	100.0	100.5	100.2	100.2	100.4	100.3	99.9	100.4	100.8	100.2	100.0	99.8	97.1	97.2	97.1	96.7
Ox.	12	12	12	6	6	6	6	8	8	8	8	8	23	23	23	23
Si	2.99	3.01	3.01	1.99	1.98	1.99	1.98	2.44	2.58	2.64	2.67	2.75	6.20	6.44	7.43	6.42
Ti	0.00	0.00	0.00	0.00	0.00	0.00	0.00	0.00	0.00	0.00	0.00	0.00	2.86	2.35	0.91	2.23
Al	1.96	1.92	1.95	0.05	0.06	0.05	0.05	1.56	1.42	1.36	1.33	1.25	0.14	0.16	0.04	0.13
Fe_{tot}	1.64	1.59	1.66	0.22	0.27	0.21	0.35	0.00	0.00	0.00	0.00	0.00	1.58	1.62	1.12	1.90
Mn	0.10	0.06	0.16	0.00	0.01	0.00	0.00	0.00	0.00	0.00	0.00	0.00	0.02	0.01	0.02	0.02
Mg	0.55	0.32	0.41	0.76	0.73	0.77	0.68	0.00	0.00	0.00	0.00	0.00	2.20	2.42	3.48	2.29
Ca	0.78	1.12	0.82	0.93	0.92	0.94	0.91	0.55	0.42	0.37	0.36	0.25	1.81	1.83	1.79	1.76
Na	0.00	0.00	0.00	0.04	0.04	0.04	0.05	0.44	0.56	0.63	0.64	0.73	0.65	0.61	0.22	0.55
K	0.00	0.00	0.00	0.00	0.00	0.00	0.00	0.00	0.00	0.00	0.00	0.00	0.09	0.08	0.02	0.09
Prp	0.18	0.10	0.13	–	–	–	–	–	–	–	–	–	–	–	–	–
Alm	0.53	0.51	0.54	–	–	–	–	–	–	–	–	–	–	–	–	–
Grs	0.25	0.36	0.27	–	–	–	–	–	–	–	–	–	–	–	–	–
Sps	0.03	0.02	0.05	–	–	–	–	–	–	–	–	–	–	–	–	–
Mg#	0.25	0.17	0.20	0.78	0.73	0.79	0.66	–	–	–	–	–	0.58	0.60	0.76	0.55
An#	–	–	–	–	–	–	–	0.56	0.43	0.37	0.36	0.26	–	–	–	–

Abbreviations after Whitney and Evans (2010).

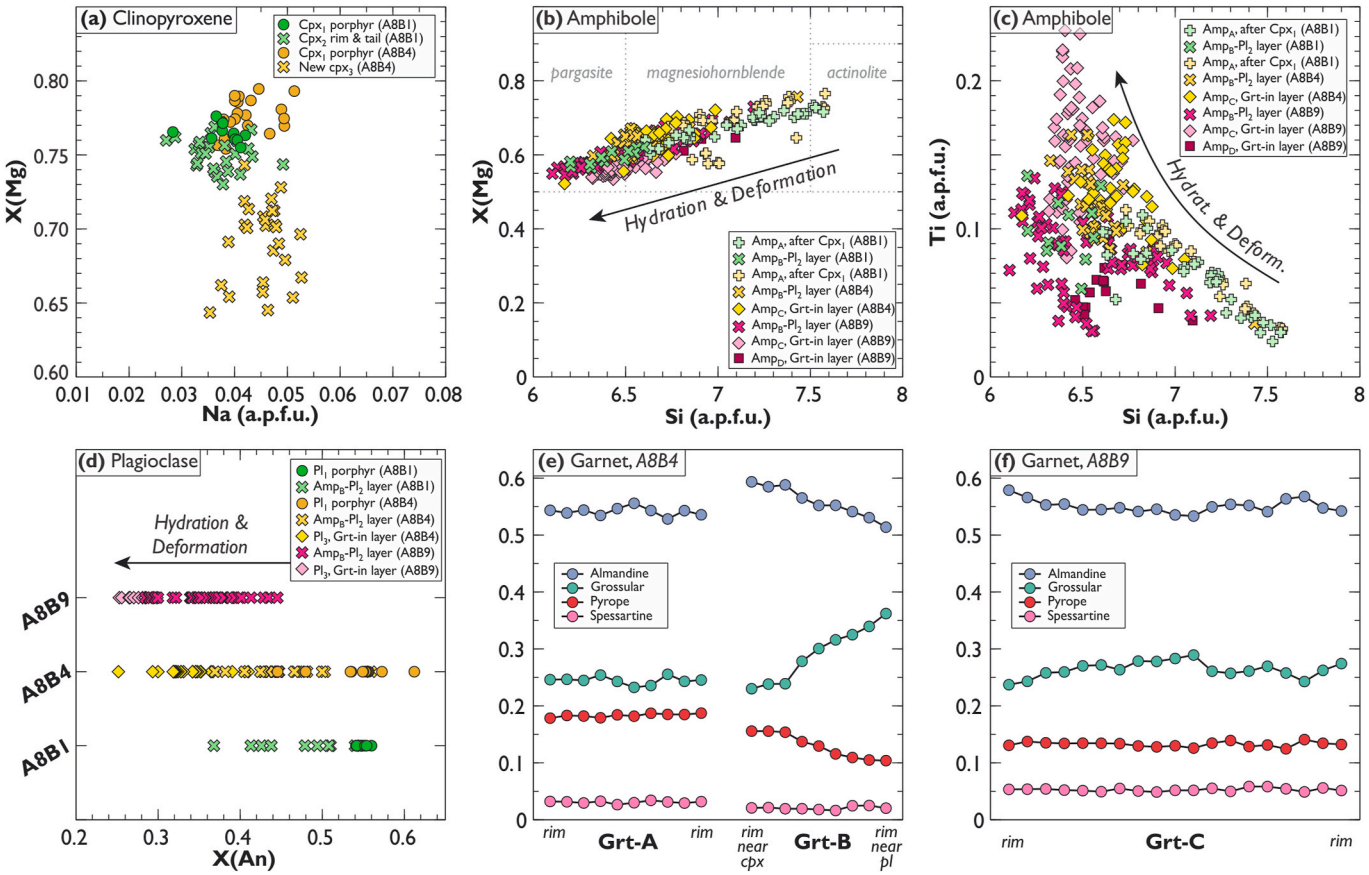

Fig. 7. Point analyses and compositions for (a) clinopyroxene, (b–c) amphibole, (d) plagioclase and (e–f) garnet from low (A8B1), mid (A8B4) and high (A8B9) high strain areas of the Kågen gabbro margins.

minerals. Garnet in the $amp_{C/D}$-rich layers of the high-strain zones shows a more homogeneous composition (Alm: 0.53–0.57, Prp: 0.13–0.14, Grs: 0.25–0.29, Sps: 0.05) that lies in-between the two garnet compositions recognized in the mid-strain zones.

Mineral chemistry exhibits local microstructural variations within the gabbro. For example, Fig. 6a and b and 7a show the variation in Mg-content between cpx_1 porphyroclasts and adjacent new cpx_2 grains. The garnet grain B in Fig. 7e shows how garnet chemistry varies when adjacent either to clinopyroxene or to plagioclase. The garnet rim around a clinopyroxene grain shows a variation in Mg content (Fig. 6c); when adjacent to plagioclase it is more depleted than the core which is adjacent to clinopyroxene and ilmenite. Fig. 6d shows a chemical map in a high strain amphibole area and how the chemistry varies between the olive green (amp_{B1}, top) and jade green (amp_{B2}, bottom) coloured amphibole (e.g. Fig. 4h and i); the olive green coloured amp_{B1} has higher Mg and Si values compared to the jade green coloured amp_{B2}. In addition the olive green coloured amp_{B1} exhibits zoning, with a decreasing of Mg and Si content from core to rim.

4.3. Pressure-temperature estimates

The amphibole-plagioclase thermo-barometry (Holland and Blundy 1994; Molina et al. 2015) yielded results for three samples of the low, mid and high strain zones (samples A8B1, A8B4 and A8B9, respectively; Table S1). The amp_B-pl_2 pairs were chosen based on textural evidence of equilibrium: immediately adjacent analyses along straight grain boundaries. The results indicate similar P-T conditions of 690 ± 25 °C and 1.05 ± 0.15 GPa for all domains (Fig. 8 inset, Table S1). Crystallization temperatures in the mid strain zone were also calculated using the garnet-clinopyroxene thermometer of Powell (1985) and Krogh (1988; Table S2). Metamorphic pairs at textural equilibrium (Mg–Fe-rich garnet and cpx_2; Fig. 6c) at textural equilibrium yielded 700 ± 25 °C at 1 GPa (Fig. 8 inset).

Peak P-T conditions of the high strain zone were additionally constrained through thermodynamic modelling. The best fit of the garnet, amphibole and plagioclase isopleths lie in the field with Amph + Cpx + Grt + Pl + Qz (without free-water), around 675 ± 25 °C and 1.05 ± 0.05 GPa (Fig. 8). The predicted mineral compositions of plagioclase, amphibole and garnet match those documented by mineral analyses in this study. The modelled temperatures and pressures are in very good agreement with those of the conventional thermo-barometry.

4.4. Crystallographic preferred orientation (CPO)

Fig. 9 shows lineation-parallel (= X-pole-figure-axis) amphibole orientation maps, CPO pole figures, and inverse pole figures (IPF) of amphibole and clinopyroxene. Clinopyroxene CPO's are only shown for low and mid strain areas as there are insufficient grains in the high strain areas to construct statistically meaningful pole figures. All individual phase maps and CPO pole figures for amphibole, clinopyroxene, plagioclase, quartz, calcite and ilmenite are available in supplementary information (Figs. S2–6).

In the low strain areas, amphibole CPO is characterised with poles to the (100) subnormal to the shear plane (XY-pole figure-section; Fig. 9), and the [001] axes subparallel to the shear direction (X-axis). The amphibole J-index is 8.26 and the M-index is 0.284 for the example low strain zone (A8B1). The misorientation axes for amphibole subgrains (2–10°) show maxima around [001] and account for >25% of misorientations (Fig. 9d). When the clinopyroxene CPO is considered alongside the amphibole CPO, the maxima are weaker but they are

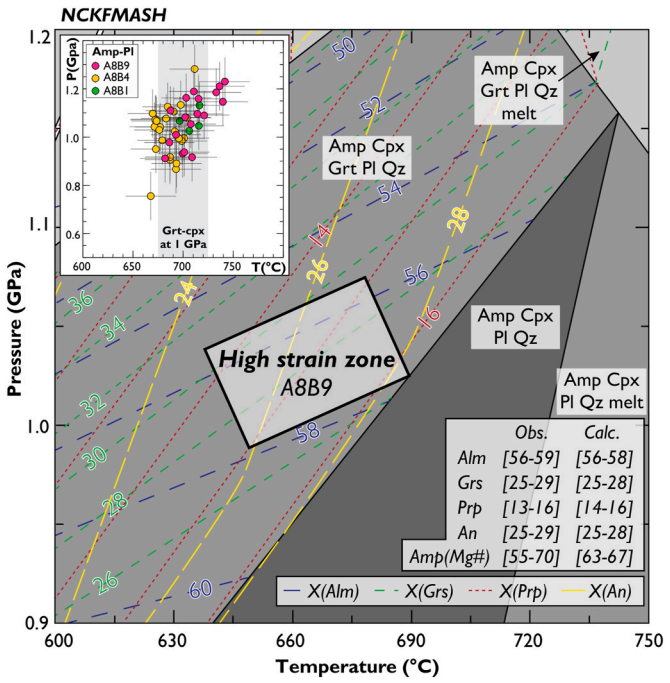

Fig. 8. Estimated P-T conditions for the high strain areas of the Kågen gabbro margins. Isopleths represent end-member garnet and anorthite compositions. P-T conditions for high strain areas of the sample are in the highlighted box, observed and calculate compositions for garnet end-members (Alm, Grs, Prp), anorthite content (An) and amphibole (Amp) are shown in the bottom right. Oxide totals for pseudosection calculation are from a XRF measurements of a high strain area: Na_2O 2.88, MgO 8.27, Al_2O_3 14.11, SiO_2 49.97, CaO 11.49, FeO 8.54, H_2O 1.15. Inset shows amphibole-plagioclase thermobarometry for low, mid and high strain areas.

orientated in similar directions. The misorientation axes for clinopyroxene subgrains is very strong around [001] and accounts for 50% of the total misorientation.

In the mid strain area the amphibole CPO has a similar fabric to the low strain area; poles to the (100) plane are subnormal to the shear plane, and the [001] axes is subparallel to the shear direction (Fig. 9). The [001] axes shows a weaker maximum but are aligned closer to the shear direction than the fabric in the low strain areas. For the mid strain zone, the amphibole J-index is 3.33 and the M-index is 0.111 (A8B4). The subgrain misorientation axes are weakly distributed between [001] and [−100], with the highest frequency of misorientations associated with subgrains. The clinopyroxene CPO in the mid strain areas is very weak and does not correlate to the amphibole CPO (Fig. 9).

In the high strain region (A8B9), the amphibole CPO exhibits a weak girdle and maximum of poles to (100) orientated normal to the shear plane, poles to (010) planes in a weak maximum subnormal to the foliation and the shear direction and the [001] direction shows a strong maximum parallel to the shear direction (Fig. 9). The amphibole J-index is 4.25 and the M-index is 0.128 for the high strain area. The amphibole subgrain misorientation axes is strong around [001] and accounts for >20% of misorientations (Fig. 9d).

The relationship between the amphibole and clinopyroxene CPO is further explored in Fig. 10 where four regions of a clinopyroxene grain with amphibole replacement has been studied. Region A shows the CPO for the clinopyroxene grain (cpx_1) and all surrounding amphibole grains. This amphibole CPO is weak and the maxima are directly related to maxima in the clinopyroxene CPO. Region B focusses on the left hand side of the main clinopyroxene grain ($cpx_{1/2}$), which has undergone more recrystallization than the right. The CPO is almost identical to region A, but is much stronger (for clinopyroxene and amphibole) than in region B. Region C shows the CPO for the right hand side of the clinopyroxene grain (cpx_1) and the amphibole (amp_A) inclusions within the grain. The CPO for this area is very strong, the amphibole and clinopyroxene maxima are in identical positions and are similar to the CPOs observed in regions A and B. The final area, region D, considers the tail of the clinopyroxene (cpx_2) where the highest amount of recrystallization and deformation has occurred. The clinopyroxene CPO for region D is very weak and does not bare a strong resemblance to the amphibole CPO. The amphibole CPO in region D is similar to the whole map amphibole CPO (region A) in the mid strain area in Fig. 9b.

The plagioclase CPO is generally weak; in low strain regions there tends to be a very weak CPO (Fig. 11a) but the CPO is not consistent between different low strain maps (see Fig. S5). The high strain area was analysed in subsets to see if there is a change in CPO strength between monophase and polyphase regions (Fig. 11c; e.g. Mehl and Hirth 2008). The CPO is weak and shows no fabric in any of the subsets, for plagioclase. Nevertheless, the amphibole for this (and all other) high strain areas shows a strong CPO with (001) normal to the shear direction and [001] parallel. The plagioclase CPO is also weak in the mid strain zone.

The quartz, calcite and ilmenite show disordered CPOs, they are either weak or strongly dominated by a few grains. Pole figures for these minerals are found in Supplementary Fig. S6.

5. Discussion

The Kågen gabbro is a 45 km^2 intrusion with a relatively unaltered and undeformed core. Deformation increases towards its margins with the Vaddas Nappe. The southern coastline of Arnøya provides a transect through the gabbro. The centre of the gabbro is relatively undeformed with a clinopyroxene, olivine, and plagioclase (±orthopyroxene) assemblage (Getsinger et al. 2013). There is localised deformation in the core of the gabbro where it is cross-cut by fluid-rich pegmatites. The deformation in the immediate vicinity to pegmatites is related to fluid released during pegmatite emplacement, the late magmatic stage of the gabbro intrusion (Getsinger et al. 2013).

Towards the edges of the gabbro (best exposed in the west), lenses of weakly deformed gabbro are surrounded by high strain margins; representing a small scale version of the general strain distribution of the whole gabbro body. The deformation at the gabbro margins overprints the largely undeformed gabbro body. This suggests the centre of the gabbro did not experience deformation during this deformation phase, it remained strong and rigid, whilst heterogeneities produced by local mineral reactions at the margins were exploited to localise deformation during emplacement of the Vaddas Nappe (Getsinger et al. 2013; Faber et al. 2019).

5.1. Mineral reactions and P-T-time of deformation

Getsinger et al. (2013) studied intrusion related deformation within the centre of the Kågen Gabbro, and observed an assemblage similar to the low strain areas in this study. The undeformed gabbro of Getsinger et al. (2013) has higher volumes of olivine and clinopyroxene, and the amphibole corona rims are absent or not well developed. Clinopyroxene is the main mafic phase of the gabbro. According to Getsinger et al. (2013) orthopyroxene in the undeformed gabbro is commonly associated with the olivine and has formed as reaction rims around it. Therefore, it is suggested that the initial alteration of the gabbro occurred via olivine reacting with plagioclase forming pyroxene (plus some spinel) rims:

$$Pl_1 + Ol \rightarrow Cpx_1 + Opx \pm Spl. \quad \text{(R1)}$$

Metamorphism of the margins of the Kågen gabbro likely occurred during emplacement and deformation of the Vaddas nappe. This main deformation event resulted in a pyroxene consuming and amphibole producing hydration reaction during nappe emplacement under changed pressure and temperature conditions:

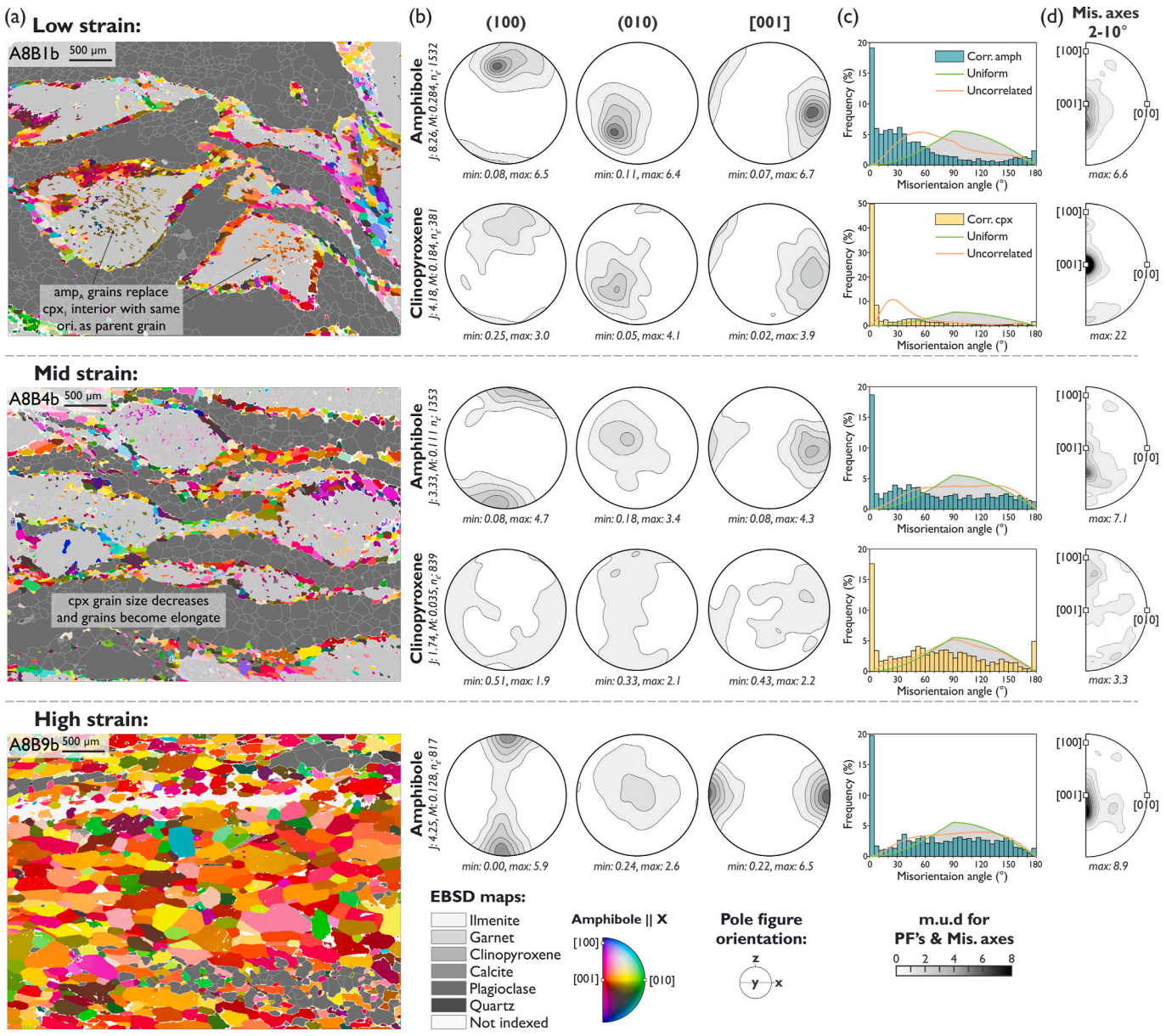

Fig. 9. (a) EBSD maps of amphibole orientations coloured parallel to the X direction, all other minerals are shown in grey. All maps are at the same scale to highlight the change in grain size and texture between the differently deformed areas. (b) Pole figures showing amphibole CPO for the low to high strain areas, and clinopyroxene CPO for the low and mid strain areas. Clinopyroxene CPO's are not plotted for the high strain area as there is less than 1% present in the map giving skewed results due to lack of grains. All pole figures are equal area, lower hemisphere projections plotted as point per grain. J-index, M-index and number of grains (n_g) is shown for each set of pole figures. (c) Distribution of misorientation angles between correlated (adjacent) pixels (histogram) and between uncorrelated pixels (orange curve) of amphibole. The uniform (green) curve corresponds to the theoretical misorientation distribution for perfectly randomly oriented crystals. (d) Amphibole and clinopyroxene inverse pole figures showing the distribution of correlated misorientation axes (between 2 and 10°). All contours are multiples of uniform distribution (m.u.d). (For interpretation of the references to colour in this figure legend, the reader is referred to the Web version of this article.)

$$Cpx_1 + Opx + Pl_1 + H_2O + Ilm \rightarrow Amp + Pl_2 + Grt + Cpx_2 \pm Qz \pm Rt. \quad \text{(R2)}$$

The least deformed parts of the Kågen gabbro exhibit some preserved assemblages (left hand side of ReactionR1) and some reacted products (right hand side of Reaction R1). The high strain regions at the margins represent the final assemblage in Reaction R2 (right hand side of R2). The low and mid strain areas show the progression of the mineral reaction R2 which is synchronous with deformation. There are remnants of clinopyroxene within some high strain amphibole layers; they represent former clinopyroxene grains that were not fully consumed in the amphibole producing reaction.

Mineral segregations show a heterogeneous distribution of reaction products, this relationship can occur through dissolution-reprecipitation (Robin 1979), poly-phase GBS (Hiraga et al. 2013) and nucleation of reaction products at microstructural or crystallographic sites associated with the reactant (Moore et al. 2015). In this study, thermodynamic modelling combined with conventional thermo-barometry show that reaction R2 took place at 690 ± 25 °C and 1.05 ± 0.15 GPa (within the uncertainties of the methods; Fig. 8), which overlaps previously established P-T conditions for the solid state cooling of the gabbro (650–900 °C, 0.7–0.9 GPa; Getsinger et al. 2013). Amphibole-plagioclase pairs show similar P-T conditions for the low, mid and high strain zones (Fig. 8 inset, Table S1). Such a result indicates that the progression of mineral reactions were directly dependent on changes in H_2O content in the bulk rock rather than a change in P-T

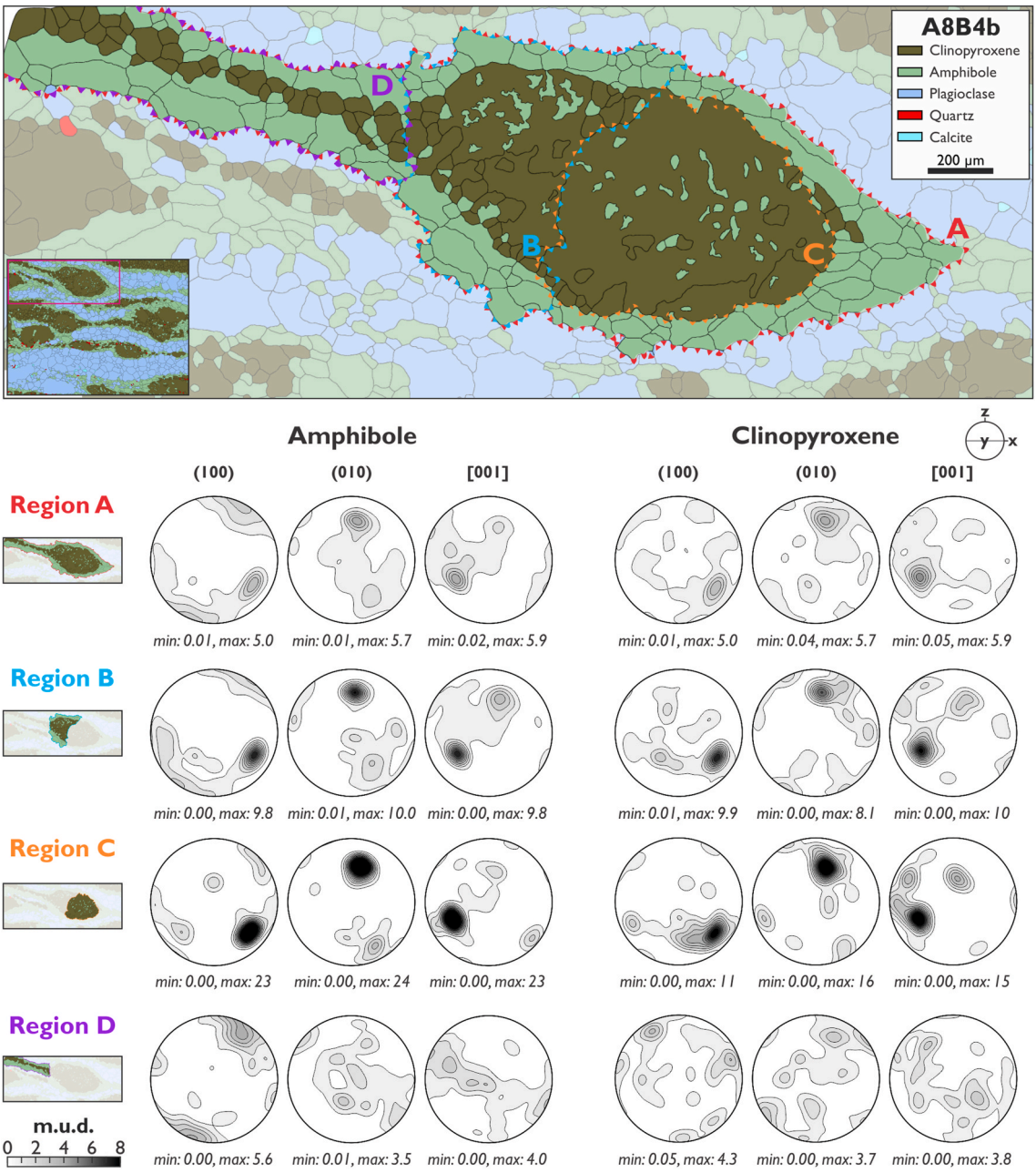

Fig. 10. EBSD phase map of a clinopyroxene grain with amphibole corona, below are CPO pole figures for selected regions associated with the clinopyroxene grain. Region A (red) includes the clinopyroxene and all grains that mantle it. Region B (blue) contains the recrystallized portion of the clinopyroxene grain and the amphibole grains that mantle and are included in the clinopyroxene grain. Region C (orange) focusses on the right hand side of the clinopyroxene grain and the amphibole inclusions within the grain. Region D (purple) includes the clinopyroxene and amphibole grains in the recrystallized tail. All pole figures are equal area, lower hemisphere projections plotted as point per grain. (For interpretation of the references to colour in this figure legend, the reader is referred to the Web version of this article.)

conditions during deformation (Finch et al. 2016; Giuntoli et al. 2018; Whyte et al. 2021).

Generally, in mid strain areas, the clinopyroxene is elongated and partially overgrown (Fig. 4f bottom) or completely replaced (Fig. 4f top) by elongated amphibole. However, in some areas the amphibole rims are absent and the clinopyroxene is mantled by garnet and occasional ilmenite (Fig. 4d and e). The absence of amphibole, a hydrated mineral, in these regions indicates a limited aqueous fluid. These observed microstructural differences together with the presence of corona structures demonstrate that local equilibrium has prevailed, most likely because fluid availability in the gabbro is extremely localised, and therefore reaction R2 is incomplete in the fluid-deficient parts. In those parts where reaction R2 is complete, as is the case for the high strain zones, aqueous fluids must have been more abundant, and therefore we suggest the high strain zones (which have formed after the low and mid strain zones) had formed fluid pathways. It is unlikely that these pathways have exploited pre-existing features in the gabbro (e.g. Mancktelow and Pennacchioni 2005; Pennacchioni and Mancktelow 2018; Ceccato et al. 2020), because such features have been interpreted as mineralised veins leading to a different type of shear zones described by Getsinger et al. (2013). Essentially, the gabbro deformation was facilitated by mineral reactions, which in turn are facilitated by fluid transport and availability, i.e. an in-situ interaction of deformation and reaction (Rutter and Brodie 1985; Fitz Gerald and Stünitz 1993; Stünitz

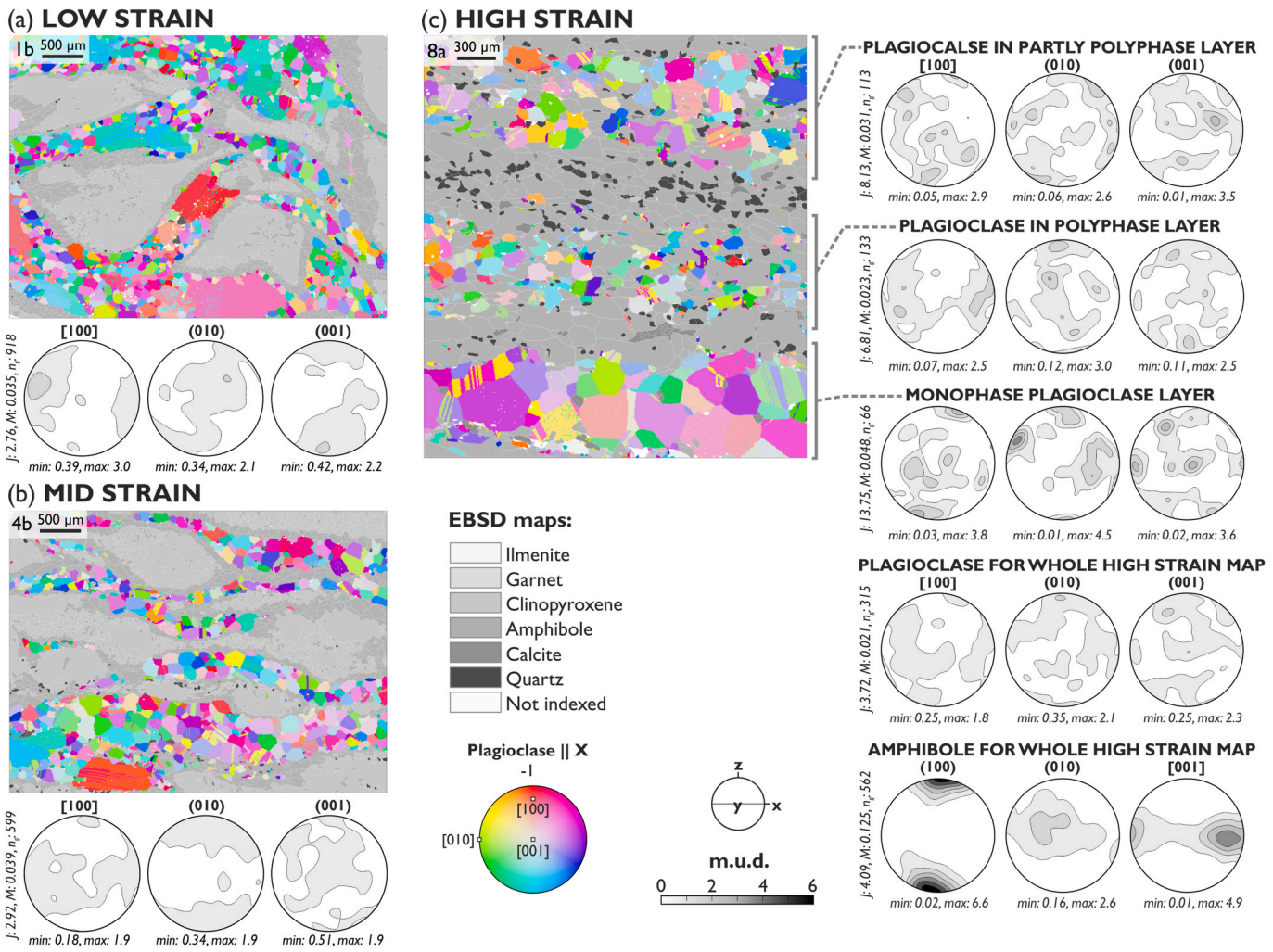

Fig. 11. EBSD map and plagioclase CPO pole figures for representative (a) low, (b) mid and (c) high strain areas. EBSD maps show plagioclase orientations coloured parallel to the X direction, all other minerals are shown in grey. Pole figures showing plagioclase CPO, for (c), additional CPO are included for polyphase and monophase areas as well as the amphibole whole map CPO is also included (maps a and b are the same area as shown in Fig. 9a and b; amphibole CPO for for these maps is shown here). All pole figures are equal area, lower hemisphere projections plotted as point per grain. J-index, M-index and number of grains (n_g) is shown for each set of pole figures.

and Fitz Gerald 1993).

The change in chemistry of new (cpx_2) vs. magmatic (cpx_1) clinopyroxene grains and the change in amphibole ($amp_{A\text{-}D}$) chemistry when it neighbours different minerals (e.g. clinopyroxene, plagioclase or garnet), demonstrates that metamorphic reactions accompanied deformation (Figs. 6 and 7). New cpx_2 grains have a different chemical composition from that of the cpx_1 porphyroclasts, indicating homogeneous nucleation. Nucleation of new cpx_2 with a different chemistry is a response to the change in P-T conditions since gabbro emplacement. The cpx_1 becomes unstable as aqueous fluid infiltrates the gabbro and enhances reaction R2. One of the consequences of the reaction-enhanced deformation is strain localisation (e.g. Rutter and Brodie 1985; Mansard et al. 2020a; 2020b). The zoning of amp_{B1} grains shows that it grew during a synkinematic reaction (Fig. 6d). The change in mineral chemistry within or between neighbouring grains demonstrates that there has been local equilibrium between phases, most likely due to local variations in fluid availability. Mineral chemistry variations in the low and mid strain zones are associated with microstructural deformation features indicating that the dominant driving potential for crystallization of clinopyroxene and amphibole has been (local) chemical equilibrium and not internal strain energy, i.e., dynamic recrystallization was not the dominant process for reconstituting the microstructures (e.g. Stünitz 1998; Okudaira et al. 2015; Giuntoli et al. 2018; Soret et al. 2019; Mansard et al. 2020a; 2020b).When the P-T conditions for the high strain areas Kågen gabbro margins (this study) and those of the more preserved inner parts of the gabbro (Getsinger et al. 2013) are considered in relationship to the surrounding Vaddas Nappe metasediments (Faber et al. 2019), the results from this study lie on a P-T path connecting them (Fig. 12). This suggests the margins of the Kågen gabbro may record the conditions for early stages of Vaddas Nappe thrusting after the gabbro emplacement, which took place at 439 ± 1 Ma (Faber et al., 2019). The deformation observed in this study is part of the same event as the deformation of the metasediments at the Vaddas-Kalak boundary (432 ± 6 Ma, $^{206}Pb/^{238}U$ ages; Faber et al., 2019), and the timing of the deformation of the gabbro margins can be constrained as between ca. 440-432 Ma.

5.2. Formation of crystallographic preferred orientation (CPO)

During deformation and metamorphism of the Kågen gabbro, the clinopyroxene CPO weakened as it destabilised, whilst the amphibole fabric strengthened as it precipitated (Figs. 9–10). Amp_A nucleation within cpx_1 grains in the low and mid strain areas indicate that initially amp_A replaced cpx_1 topotactically along cleavage planes (Fig. 4a and b,

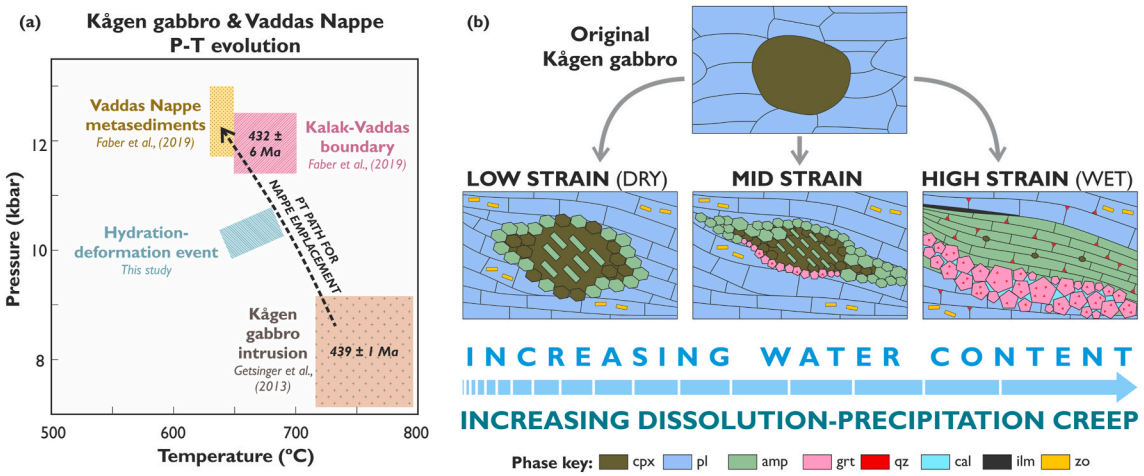

Fig. 12. (a) Composite P-T-t evolution of Kågen gabbro and Vaddas Nappe utilising P-T estimates from this study for the hydration-deformation event, Getsinger et al. (2013) for the Kågen gabbro intrusion and Faber et al. (2019) for Vaddas Nappe metasediments and Kalak-Vaddas boundary. (b) Schematic diagram of the microstructural evolution of Kågen gabbro margins when deformation occurred under differing hydration conditions. The low strain example represents 'dry' conditions where the amphibole CPO is host-controlled and inherited from clinopyroxene. The high strain example represents fluid saturated conditions where the amphibole CPO is controlled by orientated growth.

4e, 9a-b, 10c; e.g. Shannon and Rossi 1964; Handy and Stünitz 2002; McNamara et al. 2012; Moore et al. 2015). The initial topotactic replacement of cpx_1 by amp_A resulted in a direct inheritance of the cpx_1 CPO (Fig. 10) and a smaller mean grain size in low strain areas (Fig. 5a). A similar situation is inferred for the initial corona rims of amphibole on cpx_1. Thus, regions B and C in Fig. 10 show strong CPO maxima for amphibole that do not relate to the shear geometry but are instead orientated closely to that of the host clinopyroxene grain.

The amphibole fabric evolved to an orientated growth fabric that is parallel to the shear direction. The growth character of the fabric is shown by the SPO strength increasing from low to high strain areas (Fig. 5 d-f). If we consider regions A and D in Fig. 10 (including the amphibole rim and tail surrounding relict cpx_1 grain(s) and new cpx_2 grains); the poles to the (100) plane of amphibole becomes orientated subnormal to the shear direction, and the amphibole [001] axes orientated subparallel to the shear direction. These orientations do not correlate with the weaker clinopyroxene CPO's, particularly in region D (Fig. 10), where the clinopyroxene (cpx_2) CPO is very weak and does not show a distinct fabric. The morphology of the cpx_2 grains in the recrystallized tail in region D is similar to that of dynamic recrystallization during crystal plastic deformation, but chemical analysis shows that these new cpx_2 grains are compositionally different to the original cpx_1 grains (Fig. 7a) and must have formed by homogeneous nucleation due to a chemical driving potential. Therefore, we suggest the new cpx_2 grains have primarily formed during the chemical reaction when clinopyroxene adjusts its composition from cpx_1 to cpx_2. The reaction takes place alongside deformation (accommodated by dissolution-precipitation creep), progressively destroying the clinopyroxene CPO and account for the change in chemistry (e.g. Stünitz 1993; Okudaira et al. 2015; Marti et al. 2017; Stünitz et al. 2020; Mansard et al. 2020a).

Thus, during the subsequent deformation process where amphibole rims and tails develop around cpx_1 grains in the mid strain regions, amp_A started to nucleate on the cpx_1 outer boundaries with the same initial inherited clinopyroxene crystal orientation, but during consumption of the clinopyroxene by reaction, the precipitating amphibole developed a distinct fabric different from the clinopyroxene host-controlled one. The CPO of the amphibole is best interpreted as a growth-controlled fabric. Amphiboles typically are elongated in the c-axis (Deer et al. 1997), which is the fastest growth direction. As this [001] direction is aligned with the stretching direction, it is inferred that the amphibole fabric during deformation is a growth-fabric, as inferred by Giuntoli et al. (2018) and for omphacite by Stünitz et al. (2020).

Amphibole ($amp_{A,B}$) overgrows and precipitates rims and tails around cpx_1 porphyroclasts (Fig. 4a–f, 6). The CPO for these tails is progressively less related and therefore less inherited from the clinopyroxene (Fig. 10). The SPO strength for amphibole increases from low to high strain areas suggesting amphibole growth in the high strain areas is crystallographic orientation controlled (Fig. 5e). In the high strain areas, the amphibole (amp_{B-D}) CPO exhibits a maxima of (100) poles and a weak girdle subnormal to the shear direction and a strong maxima in the [001] axes parallel to the shear direction (e.g. Fig. 9). The presence of the girdle in (100) and a very strong SPO parallel to the shear direction suggests a component of rigid body rotation around [001] (Figs. 5f and 9c).

It is common to observe naturally deformed amphibole with the (100) pole aligned subnormal to the shear plane and the [001] direction aligned subparallel to the shear direction (e.g. Berger and Stünitz 1996; Imon et al. 2004; Díaz Aspiroz et al. 2007; Tatham et al. 2008; Llana--Fúnez and Brown 2012; Getsinger et al. 2013; Okudaira et al. 2015; Elyaszadeh et al. 2018; Soret et al. 2019). This fabric has been shown to occur under middle to upper amphibolite facies conditions (650–750 °C, 0.6–1 GPa), and commonly shows that amphibole grains are reoriented or grow (sub)parallel to the shear direction (Ko and Jung 2015). The primary slip vector in amphibole is < 001>, and a strong amphibole CPO with (100) plane subnormal to foliation and [001] axes parallel to lineation could suggest that (100)<001> easy slip system can be important in generating this type of CPO (Díaz Aspiroz et al. 2007). However, in the case of the Kågen gabbro there are no amphibole porphyroclasts, from which the amphibole is recrystallized, so dynamic recrystallization and thus a dislocation creep origin of the amphibole CPO can be excluded.

The amphibole CPO observed in the Kågen gabbro is similar to other natural examples, and as amphibole is only present in minor proportions (if at all) in the original gabbro (Getsinger et al. 2013), we propose that the strong fabric forms during precipitation (homogeneous nucleation) of the amphibole (e.g. Berger and Stünitz 1996; Getsinger and Hirth 2014; Giuntoli et al. 2018). The weak girdle of (100) poles in the high strain domains indicate minor rigid body rotation occurred around the [001] axes. It has been suggested that such girdles are formed through cataclastic flow forming a fine-grained matrix produced by fracturing and comminution (Imon et al. 2004; Kanagawa et al. 2008; Kim and Jung 2019). Cataclastic flow is unlikely in these samples, because (a) the confining pressures of ~1 GPa make frictional processes unlikely, and (b) the larger and uniform grain size in higher strain domains without

evidence for fracturing (Figs. 3c and 4c) do not indicate brittle processes. Instead, the rigid body rotation of amphibole grains in the Kågen gabbro is likely to have occurred via progressive rotation in a mechanically weaker plagioclase matrix, facilitated by solution transfer, precipitation and grain growth of the amphiboles as they increase in modal amount.

Plagioclase shows a decrease in the mean grain size from low to high strain areas (Fig. 5a–c). The larger grain size in low strain areas is due to the preservation of original magmatic pl_1. As deformation of the gabbro progresses, the large original grains are replaced by neo-crystallized plagioclase of a more sodic composition (pl_2; Fig. 7d). Unlike the plagioclase studied by Gardner et al. (2021) where dissolution-precipitation is identified as the dominant deformation mechanism for plagioclase in a greenschist metagabbro, Ca-plagioclase is preserved in this study. This variation is likely due to a lack of brittle fracturing in the plagioclase preventing complete albitisation. The neo-crystallization also results in a slight elongation of pl_2 grains parallel to the shear direction (Fig. 5f). The CPO of new plagioclase is weak, especially in areas where fine plagioclase grain coexist with amphibole (Fig. 11; Kruse and Stünitz, 1999; Lapworth et al., 2002; Mehl and Hirth, 2008). In the low strain regions the weak CPO is controlled by large original grains and does not represent a characteristic fabric type of crystal plasticity (Fig. 11a; e.g. Getsinger and Hirth 2014). Fig. 11c shows that the plagioclase grain size is smaller in the polyphase areas than the monophase band, suggesting that grain growth is limited in the mixed phase areas. Deformation by diffusion creep in the high strain areas is most likely accommodated by GBS that is localised in polyphase layers where phase mixing occurs between amphibole and plagioclase (Fig. 11c, polyphase layer). The weak plagioclase CPO in the high strain areas indicates a lack of crystal plasticity and the dominant deformation mechanism is inferred to be dissolution-precipitation creep (Fig. 11). Diffusion creep with GBS inhibits development of a CPO and destroys pre-existing CPO's (Elliott 1973). Unlike amphibole, there is not a strong crystallographic control on plagioclase grain shape during precipitation resulting in a lack of CPO (Getsinger and Hirth 2014). Dissolution-precipitation creep is further supported as the primary deformation mechanism active in plagioclase by plagioclase chemistry change from more anorthic in low strain areas to more albitic in high strain zones (Figs. 6c, 7d and 11c).

Quartz and calcite occur as inclusions in clinopyroxene and garnet grains or interstitially. Quartz is the more common and is usually associated with amphibole and garnet zones. This indicates there was excess silica during the metamorphic reactions to allow quartz precipitation (Fig. 6b–d, S2). The lack of CPO fabric in the quartz suggests crystal plastic deformation was not dominant during and post precipitation (Fig. S6). Calcite is occurs interstitially with a cuspate shape in amphibole zones but more commonly around garnet grains (Fig. 6b–c, S2). The cuspate calcite morphology and weak CPO fabric suggests it infilled pore space late or after in the deformation (Fig. S6). We suggest that these minerals did not undergo any crystal plasticity and precipitated late in the deformation history with no crystallographic orientation controlled growth.

5.3. Wider implications

Deformation of the Kågen gabbro margins is hypothesised to be associated with emplacement of the Vaddas Nappe on a P-T path from 690 °C and 1.05 GPa to 630 °C and 1.3 GPa (Fig. 12a; Faber et al. 2019). Crystal plastic deformation may be expected in plagioclase and clinopyroxene at such conditions (Mauler et al. 2000; Rybacki and Dresen 2004), however no evidence for dislocation creep processes is observed here. Instead, we observe a change in chemistry and stable phase assemblage between the low and high strain regions (Fig. 12b). Fluid pathways within the gabbro allowed metamorphic reactions to proceed and consequently enhanced strain localisation (e.g. Rutter and Brodie 1985; Finch et al. 2016; Whyte et al. 2021). The fluid supply was limited or infiltration was not pervasive thus allowing preservation of the dry, low strain gabbro pods. During emplacement and deformation of the Vaddas Nappe, the high strain zones formed fluid pathways and a network of anastomosing shear zones that localised deformation and left the low strain areas as dry pods (Fig. 2).

It is often assumed that new small grains in a deformed rock is the result of dynamic recrystallization (e.g. Tullis and Yund 1992; Stünitz et al. 2003), however we show that the new clinopyroxene and plagioclase grains have a different chemistry to the larger original grains (Figs. 6 and 7). This indicates dissolution-precipitation is responsible for the formation of the new grains rather than a crystal-plastic mechanism. In addition, dislocation creep is considered a fabric strengthening mechanism (e.g. strong CPO) whereas diffusion creep is fabric weakening (e.g. no CPO), but when dissolution-precipitation creep is accompanied by orientated growth, the resultant amphibole CPO is strong. Deformation experiments of plagioclase and pyroxene mixtures by Marti et al. (2017, 2018) and Mansard et al. (2020a, 2020b) showed that amphibole coronas on pyroxene were more elongated in the deformed samples. These results indicate that amphibole has accommodated displacement via dissolution-precipitation creep. As dissolution precipitation creep is a type of diffusion creep, stress exponents for this type of deformation are expected to be as low as those for diffusion creep, i.e. in the order of ñ1.

The processes that control deformation in the Kågen gabbro (e.g. DPC, rigid body rotation and GBS) are similar to those described in the garnet-clinopyroxene amphibolites formed during subduction initiation (Soret et al. 2019). Dissolution-precipitation creep alongside amphibole-forming metamorphic reactions in the Kågen gabbro are driven by variations in water activity. Fluid pathways in the gabbro resulted in strain localisation that in turn controlled the rheology (e.g. Marti et al. 2017, 2018; Soret et al. 2019; Mansard et al. 2020a; 2020b). Thus the deformation processes observed in the Kågen gabbro represent common processes controlling the development of hydrated mafic rocks, regardless of the geological setting.

6. Conclusions

Deformation at the margins of the Kågen gabbro on a P-T path from 690 °C ± 25 °C and pressures of 1.0–1.1 GPa provides a natural example of how dissolution precipitation creep facilitates the deformation of mafic rocks during concomitant mineral reactions. The dissolution part of the process takes in the reactants while the precipitation takes place in the new stable product phases. The mechanical properties of mafic rocks during deformation coupled with reactions are substantially weaker than for an assemblage of pyroxene/amphibole and plagioclase without reactions. Through chemical and microstructural analysis we have shown that metamorphic reactions primarily occurred in a fluid-rich environment, which resulted in strain localisation into the hydrating parts of the rock and subsequent weakening as metamorphic reaction progressed. Despite the strong crystal fabric and CPO in amphibole grains, dislocation creep was not the dominant deformation mechanism, instead dissolution-precipitation creep involving both, diffusion-accommodated GBS and diffusive mass transfer, has facilitated the deformation. The CPO is produced by the fastest growth direction and rigid particle rotation, i.e. by shape-factors of the precipitating amphibole. When deformation and mineral reactions occur simultaneously, strong rocks can become mechanically weak, at least transiently. Processes like dissolution-precipitation creep allow the mafic rocks to deform viscously at lower temperatures and lower stresses than expected for dislocation creep of the original constituent phases (pyroxene, amphibole, and plagioclase). Low stress exponents are expected for such a deformation.

Data availability

EBSD data for maps A8B 2b, 4b, 8a and 9b are available to download as channel text files from https://doi.org/10.17632/xhd6gs3fyc.1.

CRediT author statement

Amicia Lee: Conceptualization, Methodology, Formal analysis, Investigation, Visualization, Writing – Original Draft. **Holger Stünitz**: Conceptualization, Resources, Writing- Review & Editing. **Mathieu Soret**: Formal analysis, Investigation, Writing- Review & Editing. **Matheus Ariel Battisti***:* Formal analysis, Investigation, Writing- Review & Editing.

Declaration of competing interest

The authors declare that they have no known competing financial interests or personal relationships that could have appeared to influence the work reported in this paper.

Acknowledgements

The authors thank Amanda Getsinger for sample collection, documentation, and sample cutting. We thank Jiří Konopásek for discussions and suggestions during early chemical analysis and data processing. We thank Nicolas Rividi (Sorbonne Université, Camparis laboratory, France) for analytical support at the microprobe. We thank Toru Takeshita for editorial handling and the constructive reviews by Alberto Ceccato and Francesco Giuntoli have improved the present version of the manuscript substantially. MB thanks CAPES-Diku Project number 88881.117872/2016-01.

Appendix A. Supplementary data

Supplementary data to this article can be found online at https://doi.org/10.1016/j.jsg.2021.104505.

References

Allison, I., La Tour, T.E., 1977. Brittle deforamtion of hornblende in a mylonite: a direct geometrical analogoue of ductile deformation by translation gliding. Can. J. Earth Sci. 14, 1953–1961. https://doi.org/10.1139/e77-166.

Andersen, T.B., Austrheim, H., Sturt, B.A., Pedersen, S., Kjaersrud, K., 1982. Rb-Sr whole rock ages from Mageroy, north Norwegian Caledonides. Nor. Geol. Tidsskr. 62, 79–85.

Babaie, H.A., La Tour, T.E., 1994. Semibrittle and cataclastic deformation of hornblende-quartz rocks in a ductile shear zone. Tectonophysics 229, 19–30. https://doi.org/10.1016/0040-1951(94)90003-5.

Bachmann, F., Hielscher, R., Schaeben, H., 2010. Texture analysis with MTEX- Free and open source software toolbox. Solid State Phenom. 160, 63–68. https://doi.org/10.4028/www.scientific.net/SSP.160.63.

Berger, A., Stünitz, H., 1996. Deformation mechanisms and reaction of hornblende: examples from the bergell tonalite (central alps). Tectonophysics 257, 149–174. https://doi.org/10.1016/0040-1951(95)00125-5.

Biermann, C., van Roermund, H.L.M., 1983. Defect structures in naturally deformed clinoamphiboles - a TEM study. Tectonophysics 95, 267–278.

Brodie, K.H., Rutter, E.H., 1985. On the relationship between deformation and metamorphism, with special reference to the behavior of basic rocks. Metamorph. React. Kinet. Textures, Deform. 138–179. https://doi.org/10.1007/978-1-4612-5066-1_6.

Bunge, H.J., 1982. Texture Analysis in Materials Sciences. Buttleworth, London.

Bystricky, M., Mackwell, S., 2001. Creep of dry clinopyroxene aggregates with deformation in the dislocation creep. J. Geophys. Res. 106, 13443–13454.

Carter, N.L., Ave'Lallemant, H.G., 1970. High temperature flow of dunite and peridotite. Geol. Soc. Am. Bull. 81, 2181–2202.

Ceccato, A., Goncalves, P., Pennacchioni, G., 2020. Temperature, fluid content and rheology of localized ductile shear zones in subsolidus cooling plutons. J. Metamorph. Geol. 38, 881–903. https://doi.org/10.1111/jmg.12553.

Connolly, J.A.D., 2009. The geodynamic equation of state: what and how. Geochem. Geophys. Geosyst. 10 https://doi.org/10.1029/2009GC002540.

Connolly, J.A.D., Kerrick, D.M., 1987. An algorithm and computer program for calculating composition phase diagrams. Calphad 11, 1–55. https://doi.org/10.1016/0364-5916(87)90018-6.

Corfu, F., Gasser, D., Chew, D.M., 2014. New perspectives on the caledonides of scandinavia and related areas: Introduction. Geol. Soc. Spec. Publ. 390, 1–8. https://doi.org/10.1144/SP390.28.

Corfu, F., Torsvik, T.H., Andersen, T.B., Ashwal, L.D., Ramsay, D.M., Roberts, R.J., 2006. Early Silurian mafic-ultramafic and granitic plutonism in contemporaneous flysch, Magerøy, northern Norway: U-Pb ages and regional significance. J. Geol. Soc. Lond. 163, 291–301. https://doi.org/10.1144/0016-764905-014.

Cumbest, R.J., Drury, M.R., van Roermund, H.L.M., Simpson, C., 1989. Dynamic recrystallization and chemical evolution of clinoamphibole from Senja, Norway. Contrib. Mineral. Petrol. 101, 339–349. https://doi.org/10.1007/BF00375318.

Deer, W.A., Howie, R.A., Zussman, J., 1997. Chain silicates. In: Rock-forming Minerals, pp. 143–278.

Díaz Aspiroz, M., Lloyd, G.E., Fernández, C., 2007. Development of lattice preferred orientation in clinoamphiboles deformed under low-pressure metamorphic conditions. A SEM/EBSD study of metabasites from the Aracena metamorphic belt (SW Spain). J. Struct. Geol. 29, 629–645. https://doi.org/10.1016/j.jsg.2006.10.010.

Dimanov, A., Dresen, G., Xiao, X., Wirth, R., 1999. Grain boundary diffusion creep of synthetic anorthite aggregates: the effect of water. J. Geophys. Res. Solid Earth 104, 10483–10497. https://doi.org/10.1029/1998jb900113.

Dimanov, Alexandre, Dresen, G., 2005. Rheology of synthetic anorthite-diopside aggregates: implications for ductile shear zones. J. Geophys. Res. Solid Earth 110, 1–24. https://doi.org/10.1029/2004JB003431.

Dimanov, Alexandre, Lavie, M.P., Dresen, G., Ingrin, J., Jaoul, O., 2003. Creep of polycrystalline anorthite and diopside. J. Geophys. Res. Solid Earth 108. https://doi.org/10.1029/2002jb001815.

Dimanov, Alexandre, Raphanel, J., Dresen, G., 2011. Newtonian flow of heterogeneous synthetic gabbros at high strain: grain sliding, ductile failure, and contrasting local mechanisms and interactions. Eur. J. Mineral 23, 303–322. https://doi.org/10.1127/0935-1221/2011/0023-2110.

Dollinger, G., Blacic, J.D., 1975. Deformation mechanisms in experimentally and naturally deformed amphiboles. Earth Planet Sci. Lett. 26, 409–416. https://doi.org/10.1016/0012-821X(75)90016-3.

Drury, M.R., Urai, J.L., 1990. Deformation-related recrystallization processes. Tectonophysics 172, 235–253. https://doi.org/10.1109/IMFEDK.2013.6602261.

Elliott, D., 1973. Diffusion flow laws in metamorphic rocks. Bull. Geol. Soc. Am. 84, 2645–2664. https://doi.org/10.1130/0016-7606(1973)84<2645:DFLIMR>2.0.CO;2.

Elyaszadeh, R., Prior, D.J., Sarkarinejad, K., Mansouri, H., 2018. Different slip systems controlling crystallographic preferred orientation and intracrystalline deformation of amphibole in mylonites from the Neyriz mantle diapir, Iran. J. Struct. Geol. 107, 38–52. https://doi.org/10.1016/j.jsg.2017.11.020. Elsevier.

Faber, C., Stünitz, H., Gasser, D., Jeřábek, P., Kraus, K., Corfu, F., Ravna, E.K., et al., 2019. Anticlockwise metamorphic pressure-Temperature paths and nappe stacking in the Reisa Nappe Complex in the Scandinavian Caledonides, northern Norway: evidence for weakening of lower continental crust before and during continental collision. Solid Earth 10, 117–148. https://doi.org/10.5194/se-10-117-2019.

Finch, M.A., Weinberg, R.F., Hunter, N.J.R., 2016. Water loss and the origin of thick ultramylonites. Geology 44, 599–602. https://doi.org/10.1130/G37972.1.

Fitz Gerald, J.D., Stünitz, H., 1993. Deformation of granitoids at low metamorphic grade. I: reactions and grain size reduction. Tectonophysics 221, 299–324.

Gardner, J., Wheeler, J., Mariani, E., 2021. Lithos Interactions between deformation and dissolution-precipitation reactions in plagioclase feldspar at greenschist facies. Lithos 396–397, 106241. https://doi.org/10.1016/j.lithos.2021.106241. Elsevier B. V.

Gasser, D., Jeřábek, P., Faber, C., Stünitz, H., Menegon, L., Corfu, F., Erambert, M., et al., 2015. Behaviour of geochronometers and timing of metamorphic reactions during deformation at lower crustal conditions: phase equilibrium modelling and U-Pb dating of zircon, monazite, rutile and titanite from the Kalak Nappe Complex, northern Norway. J. Metamorph. Geol. 33, 513–534. https://doi.org/10.1111/jmg.12131.

Getsinger, A.J., Hirth, G., 2014. Amphibole fabric formation during diffusion creep and the rheology of shear zones. Geology 42, 535–538. https://doi.org/10.1130/G35327.1.

Getsinger, A.J., Hirth, G., Stünitz, H., Goergen, E.T., 2013. Influence of water on rheology and strain localization in the lower continental crust. Geochem. Geophys. Geosyst. 14, 2247–2264. https://doi.org/10.1002/ggge.20148.

Giuntoli, F., Menegon, L., Warren, C.J., 2018. Replacement reactions and deformation by dissolution and precipitation processes in amphibolites. J. Metamorph. Geol. 36, 1263–1286. https://doi.org/10.1111/jmg.12445.

Graziani, R., Larson, K.P., Soret, M., 2020. The effect of hydrous mineral content on competitive strain localization mechanisms in felsic granulites. J. Struct. Geol. 134, 104015. https://doi.org/10.1016/j.jsg.2020.104015. Elsevier Ltd.

Green, E.C.R., White, R.W., Diener, J.F.A., Powell, R., Holland, T., Palin, R.M., 2016. Activity–composition relations for the calculation of partial melting equilibria in metabasic rocks. J. Metamorph. Geol. 34, 845–869. https://doi.org/10.1111/jmg.12211.

Hacker, B.R., Christie, J.M., 1990. Brittle/ductile and plastic/cataclastic transitions in experimentally deformed and metamorphosed amphibolite. Geophys. Monogr. 56, 127–147.

Handy, M.R., Stünitz, H., 2002. Strain localization by fracturing and reaction weakening -A mechanism for initiating exhumation of subcontinental mantle beneath rifted margins. Geol. Soc. Spec. Publ. 200, 387–407. https://doi.org/10.1144/GSL.SP.2001.200.01.22.

Hiraga, T., Miyazaki, T., Yoshida, H., Zimmerman, M.E., 2013. Comparison of microstructures in superplastically deformed synthetic materials and natural mylonites: mineral aggregation via grain boundary sliding. Geology 41, 959–962. https://doi.org/10.1130/G34407.1.

Holland, T., Blundy, J., 1994. Non-ideal interactions in calcic amphiboles and their bearing on amphibole-plagioclase thermometry. Contrib. Mineral. Petrol. 116, 433–447. https://doi.org/10.1007/BF00310910.

Holland, T., Powell, R., 2003. Activity-compositions relations for phases in petrological calculations: an asymmetric multicomponent formulation. Contrib. Mineral. Petrol. 145, 492–501. https://doi.org/10.1007/s00410-003-0464-z.
Holland, T., Powell, R., 2011. An improved and extended internally consistent thermodynamic dataset for phases of petrological interest, involving a new equation of state for solids. J. Metamorph. Geol. 29, 333–383. https://doi.org/10.1111/j.1525-1314.2010.00923.x.
Imon, R., Okudaira, T., Fujimoto, A., 2002. Dissolution and precipitation processes in deformed amphibolites: an example from the ductile shear zone of the Ryoke metamorphic belt, SW Japan. J. Metamorph. Geol. 20, 297–308. https://doi.org/10.1046/j.1525-1314.2002.00367.x.
Imon, R., Okudaira, T., Kanagawa, K., 2004. Development of shape- and lattice-preferred orientations of amphibole grains during initial cataclastic deformation and subsequent deformation by dissolution-precipitation creep in amphibolites from the Ryoke metamorphic belt, SW Japan. J. Struct. Geol. 26, 793–805. https://doi.org/10.1016/j.jsg.2003.09.004.
Jessell, M.W., 1987. Grain-boundary migration microstructures in a naturally deformed quartzite. J. Struct. Geol. 9, 1007–1014. https://doi.org/10.1016/0191-8141(87)90008-3.
Ji, S., Shao, T., Michibayashi, K., Long, C., Wang, Q., Kondo, Y., Zhao, W., et al., 2013. A new calibration of seismic velocities, anisotropy, fabrics, and elastic moduli of amphibole-rich rocks. J. Geophys. Res. E Planets 118, 4699–4728. https://doi.org/10.1002/jgrb.50352.
Kanagawa, K., Shimano, H., Hiroi, Y., 2008. Mylonitic deformation of gabbro in the lower crust: a case study from the Pankenushi gabbro in the Hidaka metamorphic belt of central Hokkaido, Japan. J. Struct. Biol. 30, 1150–1166. https://doi.org/10.1016/j.jsg.2008.05.007.
Kim, J., Jung, H., 2019. New crystal preferred orientation of amphibole experimentally found in simple shear. Geophys. Res. Lett. 46, 12996–13005. https://doi.org/10.1029/2019GL085189.
Ko, B., Jung, H., 2015. Crystal preferred orientation of an amphibole experimentally deformed by simple shear. Nat. Commun. 6 https://doi.org/10.1038/ncomms7586. Nature Publishing Group.
Krogh, E.J., 1988. The garnet-clinopyroxene Fe-Mg geothermometer - a reinterpretation of existing experimental data. Contrib. Mineral. Petrol. 99, 44–48. https://doi.org/10.1007/BF00399364.
Kruse, R., Stünitz, H., 1999. Deformation mechanisms and phase distribution in mafic high-temperature mylonites from the Jotun Nappe, southern Norway. Tectonophysics 303, 223–249. https://doi.org/10.1016/S0040-1951(98)00255-8.
Kruse, R., Stünitz, H., Kunze, K., 2001. Dynamic recrystallization processes in plagioclase porphyroclasts. J. Struct. Geol. 23, 1781–1802. https://doi.org/10.1016/S0191-8141(01)00030-X.
Langdon, T.G., 2006. Grain boundary sliding revisited: developments in sliding over four decades. J. Mater. Sci. 41, 597–609. https://doi.org/10.1007/s10853-006-6476-0.
Lapworth, T., Wheeler, J., Prior, D.J., 2002. The deformation of plagioclase investigated using electron backscatter diffraction crystallographic preferred orientation data. J. Struct. Geol. 24, 387–399. https://doi.org/10.1016/S0191-8141(01)00057-8.
Leake, B.E., Woolley, A.R., Arps, C.E.S., Birch, W.D., Gilbert, M.C., Grice, J.D., Hawthorne, F.C., et al., 1997. Nomenclature of amphiboles: report of the subcommittee on amphiboles of the international mineralogical association, commission on new minerals and mineral names. Can. Mineral. 35, 219–246.
Lindahl, I., Stevens, B.P.J., Zwaan, K.B., 2005. The geology of the Váddás area, Troms: a key to our understanding of the Upper Allochthon in the Caledonides of northern Norway. Norges Geol. undersøkelse-Bull. 445, 5–43.
Llana-Fúnez, S., Brown, D., 2012. Contribution of crystallographic preferred orientation to seismic anisotropy across a surface analog of the continental Moho at Cabo Ortegal, Spain. Bull. Geol. Soc. Am. 124, 1495–1513. https://doi.org/10.1130/B30568.1.
Lloyd, G.E., Butler, R.W.H., Casey, M., Tatham, D.J., Mainprice, D., 2011. Constraints on the seismic properties of the middle and lower continental crust. Geol. Soc. Spec. Publ. 360, 7–32. https://doi.org/10.1144/SP360.2.
Mainprice, D., Nicolas, A., 1989. Development of shape and lattice preferred orientations: application to the seismic anisotropy of the lower crust. J. Struct. Geol. 11, 175–189. https://doi.org/10.1016/0191-8141(89)90042-4.
Mainprice, D., Silver, P.G., 1993. Interpretation of SKS-waves using samples from the subcontinental lithosphere. Phys. Earth Planet. In. 78 (3–4), 257–280. https://doi.org/10.1016/0031-9201(93)90160-B.
Mancktelow, N.S., Pennacchioni, G., 2005. The control of precursor brittle fracture and fluid-rock interaction on the development of single and paired ductile shear zones. J. Struct. Geol. 27, 645–661. https://doi.org/10.1016/j.jsg.2004.12.001.
Mansard, N., Stünitz, H., Raimbourg, H., Pr, J., 2020a. The role of deformation-reaction interactions to localize strain in polymineralic rocks : Insights from experimentally deformed plagioclase-pyroxene assemblages, 134. https://doi.org/10.1016/j.jsg.2020.104008.
Mansard, N., Stünitz, H., Raimbourg, H., Précigout, J., Plunder, A., Nègre, L., 2020b. Relationship between microstructures and resistance in mafic assemblages that deform and transform. Solid Earth 11, 2141–2167. https://doi.org/10.5194/se-11-2141-2020.
Marshall, D.B., McLaren, A.C., 1977. Elastic twinning in experimentally deformed plagioclase feldspars. Phys. Chem. Miner. 41, 231–240. https://doi.org/10.1002/pssa.2210410128.
Marti, S., Stünitz, H., Heilbronner, R., Plümper, O., Drury, M., 2017. Experimental investigation of the brittle-viscous transition in ma fi c rocks – interplay between fracturing , reaction , and viscous deformation. J. Struct. Geol. 105, 62–79. https://doi.org/10.1016/j.jsg.2017.10.011. Elsevier.
Marti, S., Stünitz, H., Heilbronner, R., Plümper, O., Kilian, R., 2018. Syn-kinematic hydration reactions, grain size reduction, and dissolution-precipitation creep in experimentally deformed plagioclase-pyroxene mixtures. Solid Earth 9, 985–1009. https://doi.org/10.5194/se-9-985-2018.
Mauler, A., Bystricky, M., Kunze, K., Mackwell, S., 2000. Microstructures and lattice preferred orientations in experimentally deformed clinopyroxene aggregates. J. Struct. Geol. 22, 1633–1648. https://doi.org/10.1016/S0191-8141(00)00073-0.
McNamara, D.D., Wheeler, J., Pearce, M.A., Prior, D.J., 2012. Fabrics produced mimetically during static metamorphism in retrogressed eclogites from the Zermatt-Saas zone, Western Italian Alps. J. Struct. Geol. 44, 167–178. https://doi.org/10.1016/j.jsg.2012.08.006. Elsevier Ltd.
Mehl, L., Hirth, G., 2008. Plagioclase preferred orientation in layered mylonites: evaluation of flow laws for the lower crust. J. Geophys. Res. Solid Earth 113, 1–19. https://doi.org/10.1029/2007JB005075.
Miranda, E.A., Hirth, G., John, B.E., 2016. Microstructural evidence for the transition from dislocation creep to dislocation-accommodated grain boundary sliding in naturally deformed plagioclase. J. Struct. Geol. 92, 30–45. https://doi.org/10.1016/j.jsg.2016.09.002. Elsevier Ltd.
Moghadam, H.S., Stern, R.J., Rahgoshay, M., 2010. The Dehshir ophiolite (central Iran): geochemical constraints on the origin and evolution of the inner Zagros ophiolite belt. Bull. Geol. Soc. Am. 122, 1516–1547. https://doi.org/10.1130/B30066.1.
Molina, J.F., Moreno, J.A., Castro, A., Rodríguez, C., Fershtater, G.B., 2015. Calcic amphibole thermobarometry in metamorphic and igneous rocks: new calibrations based on plagioclase/amphibole Al-Si partitioning and amphibole/liquid Mg partitioning. Lithos 232, 286–305. https://doi.org/10.1016/j.lithos.2015.06.027. Elsevier B.V.
Moore, S.J., Cesare, B., Carlson, W.D., 2015. Epitaxial nucleation of garnet on biotite in the polymetamorphic metapelites surrounding the Vedrette di Ries intrusion (Italian Eastern Alps). Eur. J. Mineral 27, 5–18. https://doi.org/10.1127/ejm/2015/0027-2414.
Morrison-Smith, D.J., 1976. Transmission electron microscopy of experimentally deformed hornblende. Am. Mineral. 61, 272–280. https://doi.org/10.1144/gsjgs.132.3.0343.
Nyman, M.W., Law, R.D., Smelik, E.A., 1992. Cataclastic deformation mechanism for the development of core-mantle structures in amphibole. Geology 20, 455–458. https://doi.org/10.1130/0091-7613(1992)020<0455:CDMFTD>2.3.CO;2.
Okudaira, T., Jeřábek, P., Stünitz, H., Fusseis, F., 2015. High-temperature fracturing and subsequent grain-size- sensitive creep in lower crustal gabbros: evidence for coseismic loading followed by creep during decaying stress in the lower crust? J. Geophys. Res. Solid Earth 120, 3119–3141. https://doi.org/10.1002/2014JB011708.
Pearce, M.A., Wheeler, J., Prior, D.J., 2011. Relative strength of mafic and felsic rocks during amphibolite facies metamorphism and deformation. J. Struct. Geol. 33, 662–675. https://doi.org/10.1016/j.jsg.2011.01.002. Elsevier Ltd.
Pennacchioni, G., Mancktelow, N.S., 2018. Small-scale ductile shear zones: neither extending, nor thickening, nor narrowing. Earth Sci. Rev. 184, 1–12. https://doi.org/10.1016/j.earscirev.2018.06.004.
Platt, J.P., Behr, W.M., 2011. Grainsize evolution in ductile shear zones: implications for strain localization and the strength of the lithosphere. J. Struct. Geol. 33, 537–550. https://doi.org/10.1016/j.jsg.2011.01.018. Elsevier Ltd.
Poirier, J.P., 1985. Creep of Crystals. Cambridge University Press. https://doi.org/10.1017/CBO9780511564451.
Powell, R., 1985. Regression diagnostics and robust regression in geothermometer/geobarometer calibration: the garnet- clinopyroxene geothermometer revisited. J. Metamorph. Geol. 3, 231–243. https://doi.org/10.1111/j.1525-1314.1985.tb00319.x.
Roberts, D., Sturt, B.A., 1980. Caledonian deformation in Norway. J. Geol. Soc. Lond. 137, 241–250. https://doi.org/10.1144/gsjgs.137.3.0241.
Robin, P.Y.F., 1979. Theory of metamorphic segregation and related processes. Geochem. Cosmochim. Acta 43, 1587–1600. https://doi.org/10.1016/0016-7037(79)90179-0.
Rooney, T.P., Riecker, R.E., Gavasci, A.T., 1975. Hornblende deformation features. Geology 3, 364–366.
Rooney, T.P., Riecker, R.E., Ross, M., 1970. Deformation twins in hornblende. Science (80-.) 169, 173–175. https://doi.org/10.1126/science.169.3941.173.
Rudnick, R.L., Fountain, D.M., 1995. Nature and composition of the continental crust: a lower crustal perspective. Rev. Geophys. 33, 267–309. https://doi.org/10.1029/95rg01302.
Rutter, E.H., 1983. Pressure solution in nature, theory and experiment. J. Geol. Soc. Lond. 140, 725–740. https://doi.org/10.1144/gsjgs.140.5.0725.
Rutter, E.H., Brodie, K.H., 1985. The permeation of water into hydrating shear zones. In: Metamorphic Reactions: Kinetics, Textures, and Deformation. Springe, New York, NY, pp. 242–250. https://doi.org/10.1007/978-1-4612-5066-1_9.
Rybacki, E., Dresen, G., 2004. Deformation mechanism maps for feldspar rocks. Tectonophysics 382, 173–187. https://doi.org/10.1016/j.tecto.2004.01.006.
Shannon, R.D., Rossi, R.C., 1964. Definition of topotaxy. Nature 202, 1001–1003. https://doi.org/10.1038/2021001a0.
Shelley, D., 1994. Spider texture and amphibole preferred orientations. Journal of Structural Geology 16 (5), 709–717. https://doi.org/10.1016/0191-8141(94)90120-1.
Siegesmund, S., Helming, K., Kruse, R., 1994. Complete texture analysis of a deformed amphibolite: comparison between neutron diffraction and U-stage data. J. Struct. Geol. 16, 131–142. https://doi.org/10.1016/0191-8141(94)90024-8.
Skemer, P., Katayama, I., Jiang, Z., Karato, S.I., 2005. The misorientation index: development of a new method for calculating the strength of lattice-preferred

orientation. Tectonophysics 411 (1–4), 157–167. https://doi.org/10.1016/j.tecto.2005.08.023.
Skrotzki, W., 1992. Defect structure and deformation mechanisms in naturally deformed hornblende. Phys. Status Solidi 131, 605–624. https://doi.org/10.1002/pssa.2211310232.
Soret, M., Agard, P., Ildefonse, B., Dubacq, B., Prigent, C., Rosenberg, C., 2019. Deformation mechanisms in mafic amphibolites and granulites: record from the Semail metamorphic sole during subduction infancy. Solid Earth Discuss. 1–36. https://doi.org/10.5194/se-2019-28.
Stünitz, H., Fitz Gerald, J.D., Tullis, J., 2003. Dislocation generation, slip systems, and dynamic recrystallization in experimentally deformed plagioclase single crystals. Tectonophysics 372, 215–233. https://doi.org/10.1016/S0040-1951(03)00241-5.
Stünitz, H., 1993. Transition from fracturing to viscous flow in a naturally deformed metagabbro. In: Defects and Processes in the Solid State: Geoscience Applications-The MacLaren Volume, pp. 121–150.
Stünitz, H., 1998. Syndeformational recrystallization - dynamic or compositionally induced? Contrib. Mineral. Petrol. 131, 219–236.
Stünitz, H., Fitz Gerald, J.D., 1993. Deformation of granitoids at low metamorphic grade. II: granular flow in albite-rich mylonites. Tectonophysics 221, 299–324. https://doi.org/10.1016/0040-1951(93)90164-F.
Stünitz, H., Neufeld, K., Heilbronner, R., Finstad, A.K., Konopásek, J., Mackenzie, J.R., 2020. Transformation weakening: diffusion creep in eclogites as a result of interaction of mineral reactions and deformation. J. Struct. Geol. 139 https://doi.org/10.1016/j.jsg.2020.104129.
Tatham, D.J., Lloyd, G.E., Butler, R.W.H., Casey, M., 2008. Amphibole and lower crustal seismic properties. Earth Planet Sci. Lett. 267, 118–128. https://doi.org/10.1016/j.epsl.2007.11.042.
Terry, M.P., Heidelbach, F., 2006. Deformation-enhanced metamorphic reactions and the rheology of high-pressure shear zones, Western Gneiss Region, Norway. J. Metamorph. Geol. 24, 3–18. https://doi.org/10.1111/j.1525-1314.2005.00618.x.
Tullis, J., 1983. Deformation of feldspars. In: Feldspar Mineralogy, pp. 297–323.
Tullis, J., Yund, R.A., 1992. The brittle-ductile transition in feldspar aggregates: an experimental study. Int. Geophys. 51, 89–117. https://doi.org/10.1016/S0074-6142(08)62816-8.
van Roermund, H.L.M., Lardeaux, J.M., 1991. Modification of antiphase domain sizes in omphacite by dislocation glide and creep mechanisms and its petrological consequences. Mineral. Mag. 55, 397–407. https://doi.org/10.1180/minmag.1991.055.380.09.
Wheeler, J., 1992. Importance of pressure solution and coble creep in the deformation of polymineralic rocks. J. Geophys. Res. Solid Earth 97, 4579–4586. https://doi.org/10.1029/91JB02476.
White, R.W., Powell, R., Holland, T., Johnson, T.E., Green, E.C.R., 2014. New mineral activity-composition relations for thermodynamic calculations in metapelitic systems. J. Metamorph. Geol. 32, 261–286. https://doi.org/10.1111/jmg.12071.
Whitney, D.L., Evans, B.W., 2010. Abbreviations for names of rock-forming minerals. Am. Mineral. 95, 185–187. https://doi.org/10.2138/am.2010.3371.
Whyte, A.J., Weller, O.M., Copley, A.C., St-Onge, M.R., 2021. Quantifying water diffusivity and metamorphic reaction rates within mountain belts, and their implications for the rheology of cratons. Geochem. Geophys. Geosyst. 22, 1–24. https://doi.org/10.1029/2021gc009988.